# General Disclaimer

One or more of the Following Statements may affect this Document

- This document has been reproduced from the best copy furnished by the organizational source. It is being released in the interest of making available as much information as possible.

- This document may contain data, which exceeds the sheet parameters. It was furnished in this condition by the organizational source and is the best copy available.

- This document may contain tone-on-tone or color graphs, charts and/or pictures, which have been reproduced in black and white.

- This document is paginated as submitted by the original source.

- Portions of this document are not fully legible due to the historical nature of some of the material. However, it is the best reproduction available from the original submission.

Produced by the NASA Center for Aerospace Information (CASI)
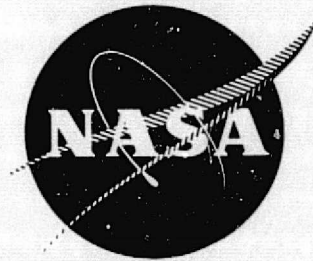
THE ION-OPTICS OF A TWO-GRID ELECTRON-BOMBARDMENT THRUSTER

by

Graeme Aston

Approved by

Paul J. Wilbur

May 1976

Department of Mechanical Engineering
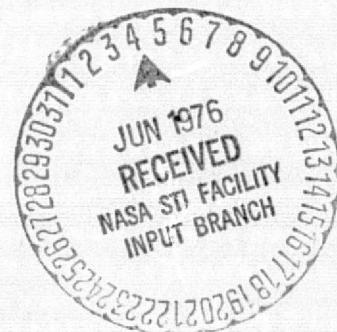Colorado State University
Fort Collins, Colorado

TABLE OF CONTENTS

TABLE OF CONTENTS

LIST OF TABLES

LIST OF FIGURES

LIST OF FIGURES

INTRODUCTION

Extracting a broad, collimated, ion[*] beam from a low density plasma represents a difficult problem in ion-optical design. There have been attempts to design efficient ion extraction systems mathematically [1-5], however, the theoretical considerations involved make it difficult to obtain reliable solutions. The production of a broad ion beam is important to the development of ion thrusters designed for the propulsion of space vehicles. These devices obtain thrust by ejecting large numbers of ions at high velocities over extended periods of time. An accurate knowledge of the distribution of ion trajectories (the beam profile) is of considerable importance when applying ion thrusters to actual mission situations because of the thrust degradation associated with off-axis trajectories. Broad ion beams are also important in a variety of ground based ion sources. Although thrust is not important in these ground applications, there are other reasons for preferring a well collimated beam.

This study deals with the effect of variations in extraction geometry and operating conditions of the extraction system on the ion beam obtained from an ion source. The results of this study are applicable to both thrusters and a variety of ground-based ion sources.

---

[*] Since this work deals only with positive ions, the term "ion" is used with the exclusive meaning "positive ion."

Chapter 1

ION BEAM FORMATION

Grid System Operation

The ion extraction system employed for this study was the two
grid accelerator geometry common to most ion propulsion devices.
Figure 1-1 depicts a portion of this multiple aperture system, showing
the formation of an ion beamlet. The variation in electrical potential
associated with the grid geometry of Figure 1-1 is shown in Figure 1-2.
The grid system parameters and symbols indicated on these figures are
listed below:

ℓ_g = separation between screen and accelerator grids

d_s = diameter of screen apertures

d_a = diameter of accelerator apertures

t_s = thickness of screen grid

t_a = thickness of accelerator grid

ℓ_e = Kaufman effective acceleration length [5]

α = ion beam divergence angle

V_t = total accelerating voltage

V_n = net accelerating voltage

R = net-to-total accelerating voltage ratio.

A low density plasma is generated within a discharge chamber at a
potential a few tens of volts above that of the screen grid, which is
itself usually elevated to a high positive potential with respect to
ground [Figure 1-2]. The ions produced move toward the screen grid as
a result of random thermal motion and slight potential variations

2
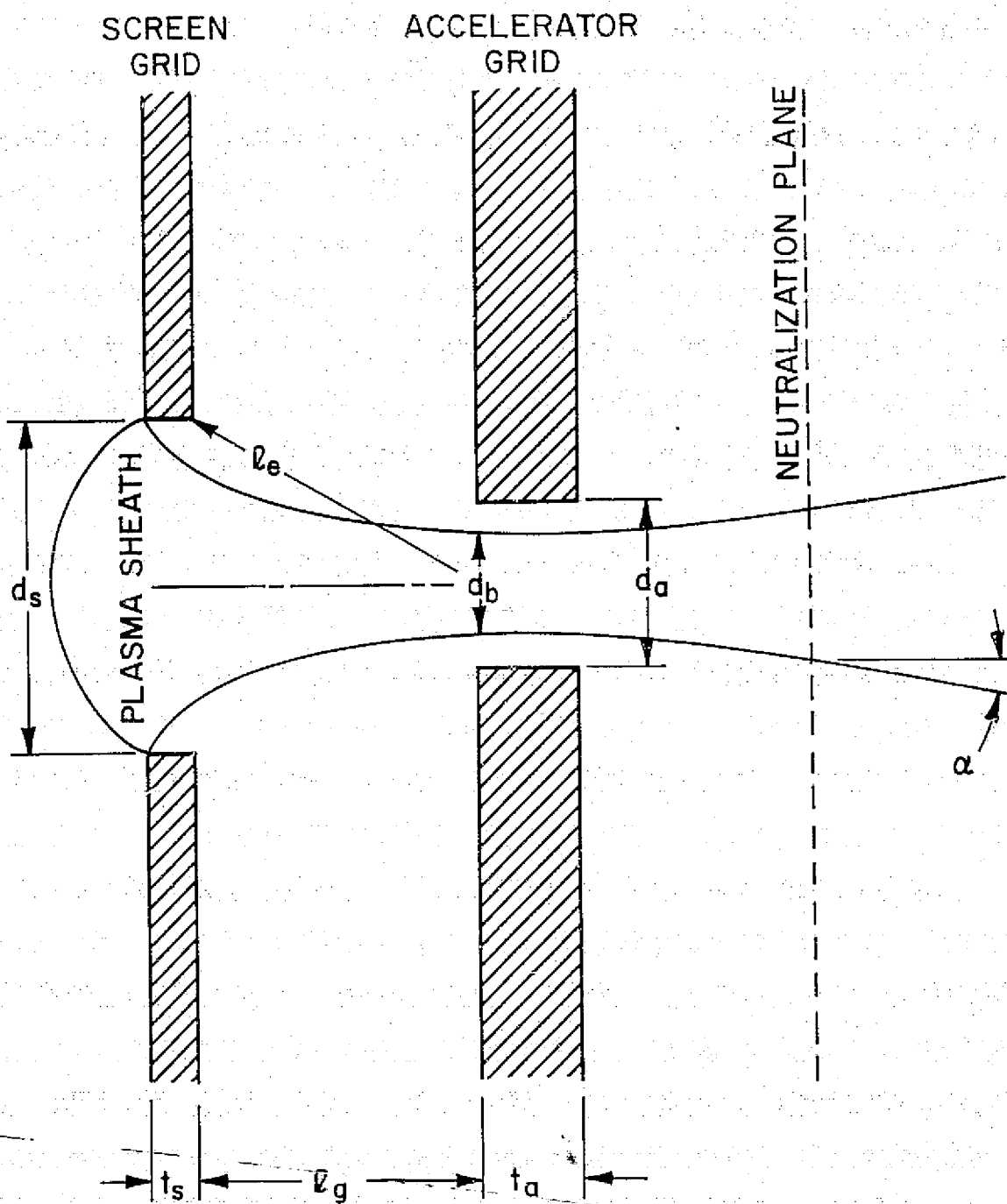
GRID SYSTEM PARAMETERS

FIGURE 1-1
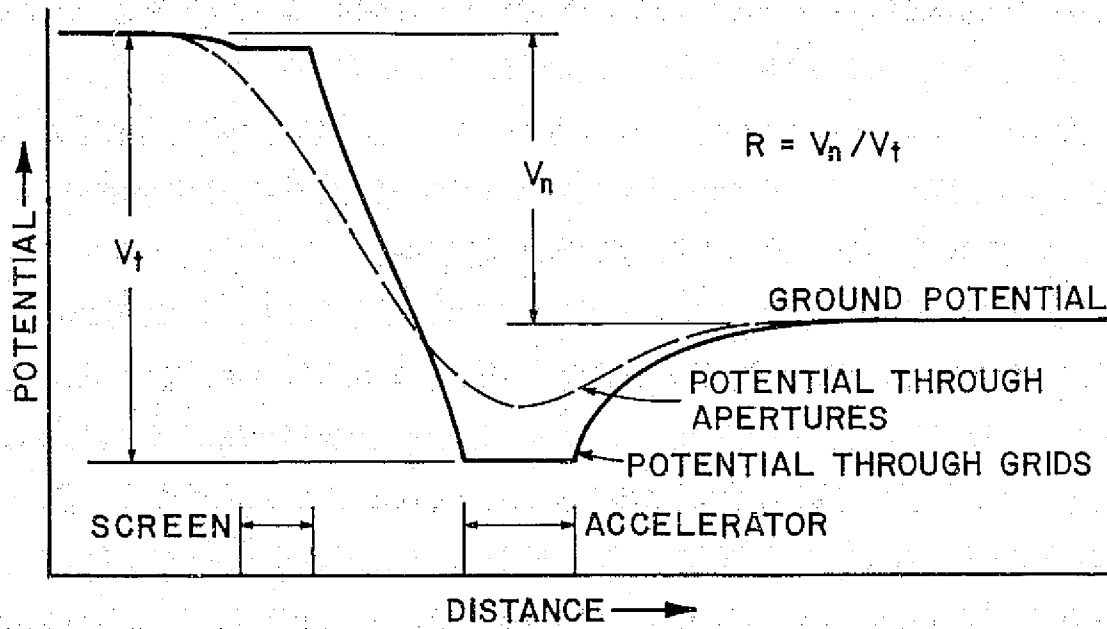
ACCELERATOR POTENTIAL VARIATION

FIGURE 1-2

within the plasma. At the entrance to the screen hole a stable plasma sheath is formed [Figure 1-1] and the ions exit from its surface with the characteristic Bohm velocity [6].

Ion acceleration is achieved because of the potential difference between the plasma and the accelerator grid [Figure 1-2]. Depending upon the amount of focusing that occurs and the subsequent ion beamlet diameter, d_b, most of the ions will pass through the accelerator grid and be expelled into the region beyond. This region is usually re-ferred to as the downstream side of the grids, which for a flight thruster represents the vacuum of space.

Ion Beam Divergence

Ion thrusters, being inherently low thrust devices, must produce a highly collimated ion beam for efficient operation. The final tra-jectory imparted to each beam ion is a result of the focusing it receives while passing through the grids and defocusing it experiences once it leaves the accelerator system. While the former mechanism is readily understood in terms of the equipotential distribution that exists between an operating grid set [1-4], the factors controlling defocusing are less well known and warrant some discussion.

As the accelerated ions leave the grid system, electrons are in-jected into the beam to maintain a neutral charge efflux. These neutralization electrons, as they are called, rapidly spread through-out the beam producing a neutral plasma. Because of the negative po-tential on the accelerator grid, neutralization electrons coming within a finite distance of the accelerator holes are repulsed by electro-static forces. The result is a neutralization surface created

slightly downstream from the accelerator grid. For multiaperture grid systems this surface is roughly planar [Figure 1-1].

Between the neutralization plane and accelerator holes the ions are in a region of decelerating electric field directed towards the negative accelerator grid [Figure 1-2]. Although the deceleration incurred is less than the acceleration imparted by the grid set, it is still sufficient to defocus the ion trajectories significantly. However, once these ions reach the neutralization plane, electrostatic shielding by the beam plasma nullifies the accelerator grid's effect and little additional change in ion trajectories occurs. A measure of the overall ion beam divergence is given by the angle α [Figure 1-1].

It is apparent that the ion beam divergence angle is one parameter important in determining the ability of a particular grid geometry to produce the desired ion beam collimation. There is however another less obvious quantity which is of considerable interest for space flight applications. This is the ion beam divergence factor, f_d, which is a ratio of the net axial thrust produced by the divergent ion beam to the thrust produced if the ion beam were perfectly collimated. These two quantities were the calculated parameters (based on experimental measurements) of primary interest to this study.

Theoretical Considerations

There exists a space charge flow limit to the ion current that can be extracted from an accelerating system of this kind. Space charge effects on accelerator system performance can be determined by solving Poisson's equation for a single aperture grid geometry

$$\nabla^2 V = -\frac{\rho}{\varepsilon_0} \qquad (1-1)$$

where V is the electrostatic potential and ρ is the charge density of the ions in the beam. Assuming one dimensional flow between parallel plane electrodes and zero electric field across the plasma sheath emitting surface, Equation (1-1) yields Child's current density law [7]

$$j = \frac{4\varepsilon_0}{9} \left(\frac{2q}{m}\right)^{1/2} \frac{V_t^{3/2}}{\ell^2} \qquad (1-2)$$

Here j is the ion current density in the beam, $\frac{q}{m}$ is the ion charge-to-mass ratio, V_t is the total accelerating potential at a distance ℓ downstream of the screen hole sheath and ε_0 is the permittivity of free space.

The ability of a grid set to extract the maximum ion current per hole for the minimum total accelerating voltage is a measure of its performance. This quantity is referred to as perveance and is defined by

$$\left(\frac{J}{V_t^{3/2}}\right) = \frac{\pi\varepsilon_0}{9} \left(\frac{2q}{m}\right)^{1/2} \left(\frac{d_s}{\ell}\right)^2 \ . \qquad (1-3)$$

Here the assumption has been made that the ion current J is emitted from a plasma sheath whose area is constant, and approximately equal to that of the screen hole. For this study the acceleration distance ℓ is described by the Kaufman effective acceleration length ℓ_e [5], where

$$\ell_e = \left(\ell_g^2 + \frac{d_s^2}{4}\right)^{1/2} \qquad (1-4)$$

Actual grid set performance then can be expressed better in terms of a "normalized perveance per hole," which is defined as

$$\left(\frac{J}{V_t^{3/2}}\right)\left(\frac{\ell_e}{d_s}\right)^2 = \frac{\pi\varepsilon_0}{9}\left(\frac{2q}{m}\right)^{1/2} \tag{1-5}$$

Equation (1-5) indicates that a theoretical limit governs the maximum obtainable normalized perveance per hole for a particular propellant. Normalized perveance per hole will be used to describe the ion extraction performance of each grid set investigated.

Chapter 2

APPARATUS

Ion Source

For this study, a simple mildly-divergent-field 8-cm electron-bombardment ion source was constructed and operated on argon propellant. Tungsten wire filaments were used as both the main and neutralizer cathode emitters. The magnetic field was derived from a long solenoidal winding extending the length of the discharge chamber, with an additional coil winding positioned at the chamber's rear. The geometry was such that the field at the front of the discharge chamber was 60% that of the rear. A cylindrical anode was employed and non-magnetic stainless steel construction used throughout. Figure 2-1 illustrates the basic ion source design with associated power supplies and instrumentation. Further design details and operating characteristics for this type of source can be found in the literature [8-10].

All source operation was conducted in a 30-cm diameter pyrex bell jar pumped by a 10-cm oil diffusion pump in series with a mechanical pump. The argon flow rate into the source was sensed by a Hastings mass flow meter and displayed on a digital readout.

Grid Construction

The screen and accelerator grids were made from thin sheet graphite. This material has a low ion-sputter erosion rate and a low coefficient of thermal expansion. In addition, because it could be machined easily and was readily available in the desired thicknesses, graphite was particularly attractive for use as a grid material.

9
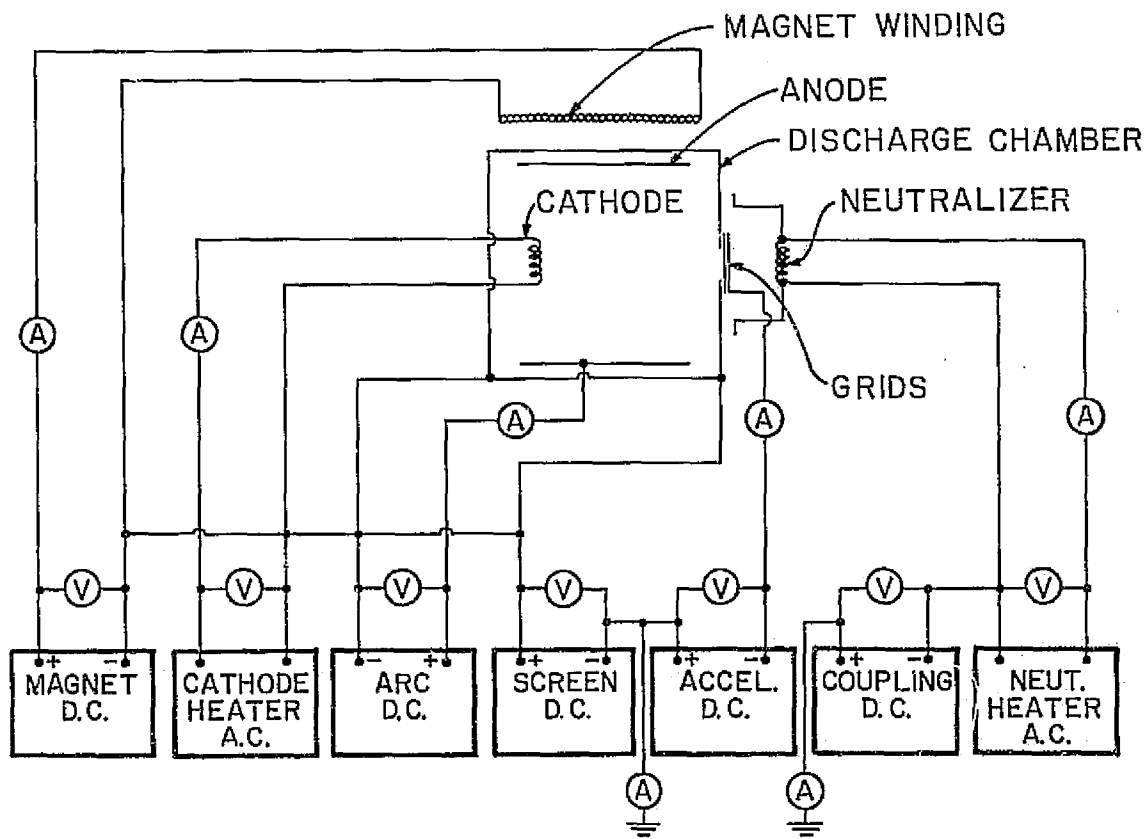
ION SOURCE POWER SYSTEM SCHEMATIC

FIGURE 2-1

The grid aperture pattern employed consisted of a nineteen hole hexagonal array with a center-to-center hole spacing of 2.54 mm. It was felt that this number of holes would adequately model the adjacent hole interactions found in full size grid systems. Five-centimeter square graphite plates containing the grid pattern were positioned on a masking plate which covered most of the downstream end of the discharge chamber. The array of holes covered only a small portion of the cross section near the axis, which insured ion extraction from a near uniform plasma. Calculations predicted that the greatest possible spatial variation in discharge chamber ion density across the grid open area would be less than 5%.

Variable grid separation was achieved by using thin mica washers (0.254 mm thick). These were replaced after each data run to avoid insulation breakdown and large leakage currents. The grid sets were fastened together using four stainless steel bolts which were properly insulated to prevent direct shorting. Alignment of the screen and accelerator grids was accomplished by hand beneath a large illuminated magnifying glass; this straightforward technique was found to produce the degree of reliability desired. Grid separation could be checked when they were cold, but not while the source was operating and the grids were hot. While some grid warpage could occur during operation, the magnitude of this warpage should be small because the grids were carbon and the greatest distance between grid supports was less than 2 cm.

Ion Beam Measurement

(a) Beam Composition

The ion beam produced by an electron-bombardment source is composed mainly of primary beam ions, that is ions which have received the

maximum energy that can be imparted by the grids. However, the ion beam also contains a small multi-energy ion distribution produced as a result of primary beam ions undergoing charge exchange reactions with escaping neutral propellant atoms. This exchange occurs in regions between and downstream of the grids [11-12].

Charge exchange ions produced between the grids, and having sufficient energy to escape, are commonly called group 2 ions (this designation is adopted from Kerslake et al. [11]). The acceleration they receive and their resultant energy depends upon where they were created between the grid set. Some may have energies up to hundreds of electron volts. Because of the improper focusing group 2 ions receive subsequent to their formation, most have severe off-axis trajectories and are quickly lost from the primary ion beam. In contrast, group 4 charge exchange ions originate downstream of the grids and so are created in a near field free region. The small electric fields which do exist within the ion beam are a result of plasma density variations. These fields direct the group 4 ions further downstream, imparting to them a few electron volts of energy. The potential gradients are usually fairly uniform along the beam axis; however, they become more non-uniform and have major off-axis components as the beam edge is approached. The result is an ill defined beam edge caused by group 4 ion migration to regions outside the primary ion beam.

(b) Faraday Probe Rake

The basic ion beam detection apparatus used the Faraday probe to sense beam ion currents [13]. Typically, an individual Faraday sensor consists of a small flat plate electrode which is biased a few volts negative relative to ground and is usually positioned within the beam plasma at some point downstream of the ion source. Neutralization

electrons are reflected from the sensor's surface because of its nega-
tive potential, leaving the ion beam impingement to be recorded as a
net positive current.

Distortion of the primary ion beam profile, caused by the presence
of group 4 ions in the beam plasma, made it necessary to modify the usual
Faraday probe design so that only primary beam ions would be detected.
To accomplish this, a second electrode of large transparency (stainless
steel mesh) was positioned a few millimeters in front of the Faraday
sensors. This second electrode was held negative with respect to ground
while the probes were biased a few volts positive above ground.

During probe rake operation, neutralization electrons are reflected
by the probe screen. This occurs because the mesh size, approximately
1.2 mm square, is less than the Debye shielding distance for the maximum
electron-ion densities found in the beam. The high energy of the pri-
mary beam ions, several hundred electron volts, allows them to pass
through the screen (the mesh and an open area fraction of approximately
70% which necessitated a correction for direct interception), and impinge
essentially undeflected on the probes. However, the much lower energy
group 4 ions have their trajectories seriously affected by the retarding
electric field between the screen and probe surfaces. Thus, most group
4 ions are deflected into the screen where they are conducted away from
the plasma. The actual effectiveness of the screened probe in suppress-
ing group 4 ions is further discussed in Appendix I.

In practice, twenty probes were used with a common probe screen
electrode. The probes were mounted in line (with a center-to-center
spacing of one centimeter) on a moveable support cradle, allowing them
to be positioned along the beam axis. Basic construction details are
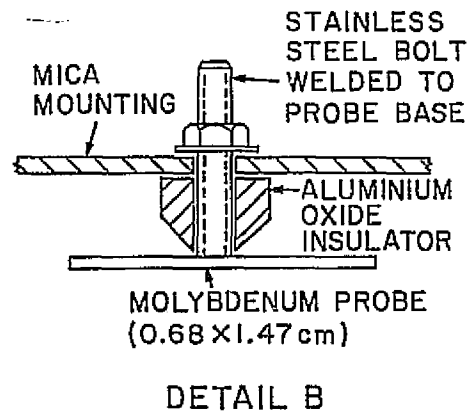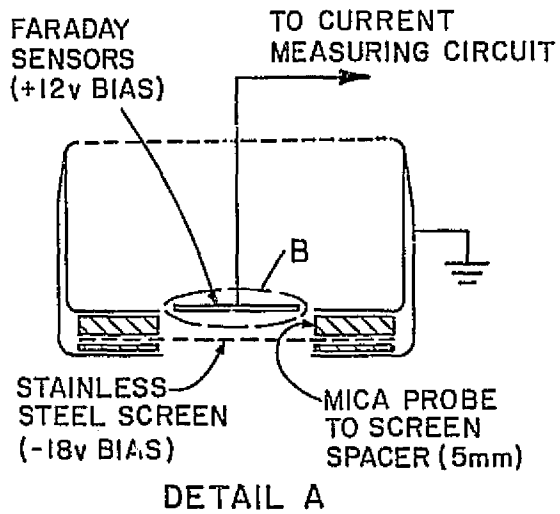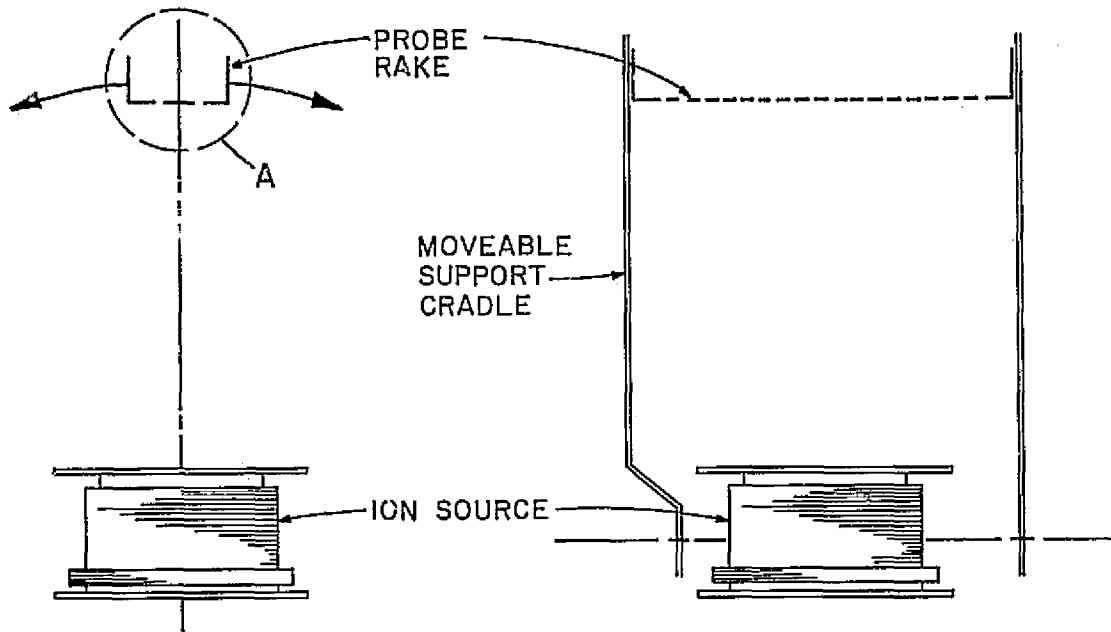
FARADAY PROBE RAKE CONSTRUCTION DETAILS

FIGURE 2-2

shown in Figure 2-2. Molybdenum was used for the ion detection surface of each probe because of its low secondary electron emission characteristics as a result of direct ion impingement. Selection of the screen and probe bias potentials resulted from a systematic investigation to determine the combination resulting in current densities which went to zero but did not go negative at the edges of the beam.

Figure 2-3 illustrates the instrumentation used to monitor individual probe currents. A digital voltmeter, measuring the voltage drop across a precision resistor, covered the higher ranges of probe current while two sensitive microammeters were used for the lower current ranges. Only the probe being read was biased positive, the surrounding probes and supporting structure were at ground potential; this insured minimal ion beam distortion due to secondary electron losses from, and group 4 ion collection on, the probe being read.
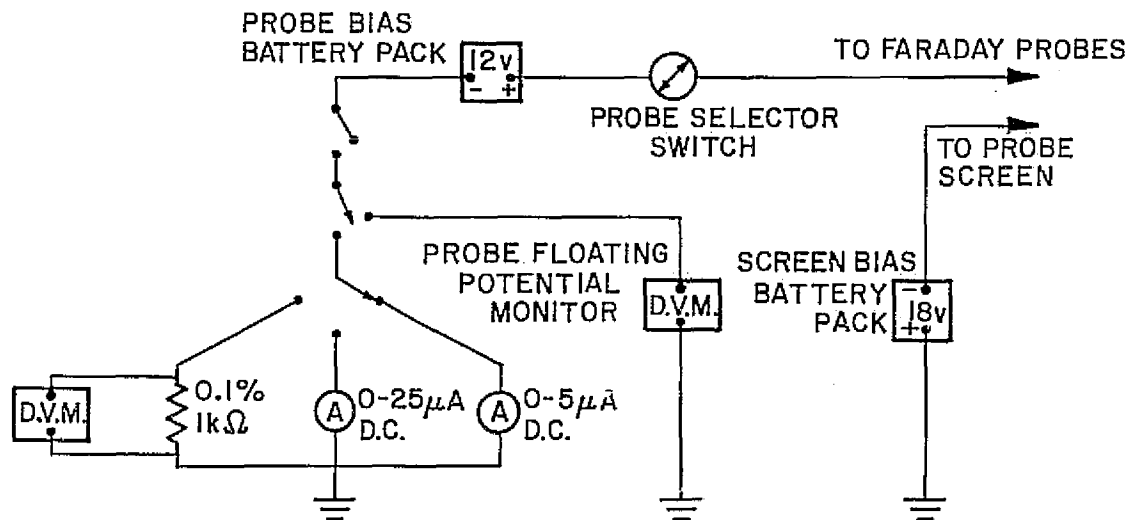
FARADAY PROBE RAKE INSTRUMENTATION SCHEMATIC

FIGURE 2-3

Chapter 3

PROCEDURE

Ion Source Operation

The ion source was operated with variable beam current (controlled by cathode emission) at the following conditions:

Arc voltage	40 V
Magnet current	7 A
Neutralizer coupling voltage	0 V
Propellant flow rate	7 mA (equivalent)

The arc voltage was set at 40 V to keep the production of doubly charged argon ions to negligible levels within the discharge chamber. A magnet current of about 7 ampere was found to be near optimum for the source used. Going beyond this value produced no additional increase in beam current. The neutralizer geometry consisted of a tungsten loop which completely surrounded the beam downstream of the accelerator grid. Because of the large loop size relative to the ion extraction area, efficient current neutralization could be obtained with the filament at ground potential. A propellant flow rate of 7 mA was the minimum which would give a stable discharge over the operating range of beam currents.

Constant operating conditions (no thermal transients) was usually achieved within half an hour after start-up; the collection of data was begun soon thereafter. Beam current was controlled for the tests by adjusting the refractory cathode current and hence electron mission. Each grid set geometry investigated was operated over a range of emission levels up to the maximum beam current obtainable from the grids; the approach to this maximum was characterized by a rapid increase in accelerator.

impingement current and a negligible increase in beam current. The effect of the net-to-total accelerating voltage ratio, R, on the ion beam profile was also investigated. Table 1 lists the range of voltage ratios used.

Table 1: GRID VOLTAGES

V_{screen}	$|V_{accel}|$	V_{net}	V_{tot}	$R = \dfrac{V_{net}}{V_{tot}}$
255	300	300	600	0.500
375	180	420	600	0.700
495	60	540	600	0.900

Here $V_{net} = V_{screen} + V_{sheath} + V_{arc}$,

$$V_{tot} = |V_{accel}| + V_{net}$$

and V_{sheath} was assumed to be 5 volts. The bell jar pressure varied from 5.5×10^{-5} to 8.5×10^{-5} torr during source operation.

Obtaining a Beam Profile

After obtaining stable source operation, the probe rake was moved through the ion beam with one of the central probes sensing ion current. The position where that probe indicated a maximum current defined the center of the beam. Each beam profile was obtained by taking a set of twenty ion current density measurements, corresponding to the individual ion current received by each probe as a function of its position normal to the beam axis. These data were given as input to a computer program which calculated the ion beam divergence angle enclosing 95% of the total integrated beam current and the ion beam divergence factor associated with the entire current density profile. Further details of this analysis technique are discussed in Appendix II.

Chapter 4

EXPERIMENTAL RESULTS

Grid Geometry Variation

Investigation of grid geometry variations on ion-optical perform-
ance* was done by independently varying the grid separation distance,
ℓ_g, accelerator aperture diameter, d_a, screen grid thickness, t_s and
accelerator grid thickness, t_a. To non-dimensionalize the geometrical
grid parameters they were divided by the screen hole diameter, d_s,
which remained at 0.206 cm throughout this study. Although the ion
source was operated on argon propellant, normalized perveance is cal-
culated for operation with mercury, since mercury is the propellant of
principle interest for space flight thrusters. The theoretical limit
of obtainable normalized perveance per hole, using mercury, can be
found from Equation (1-5) and is equal to 3.03×10^{-9} amp/volt$^{3/2}$.

The reliability of the data contained within this chapter was
verified by repeatedly testing various grid set geometries at different
times. The results of these tests showed a maximum variation in ion
beam divergence angle of ± 0.5 degrees and a maximum variation in ion
beam divergence factor of ± 0.001. A tabular listing of the experi-
mental results presented graphically in this chapter can be found in
Appendix III.

---

* Ion-optical performance is defined as the degree of ion beam col-
limation. A grid set geometry said to have "good ion-optical
performance" produces an ion beam characterized by low beam
divergence angles and high beam divergence factors.

(a) Effect of Grid Separation

Increasing the grid separation ratio $\frac{\ell_g}{d_s}$ and keeping all other geometrical parameters constant results in significant decreases in the ion beam divergence angle, α, with corresponding increases in the ion beam divergence factor, f_D, Figure 4-1A. Qualitatively, all curve trends are similar with only slight variations in the limit of obtainable normalized perveance per hole[*]. In all cases the minimum beam divergence angle and the maximum beam divergence factor occur about a normalized perveance per hole of 1.0×10^{-9} amp/volt$^{3/2}$. This similarity in curve shape for different values of ℓ_g indicates that the use of normalized perveance (with ℓ_e as the acceleration distance) is effective in correlating performance of different geometries. Figure 4-1B shows a comparison of these data with similar geometries investigated theoretically by Kaufman [5]. Kaufman's results agree qualitatively with experimental trends, but the quantitative agreement is poor.

(b) Effect of Accelerator Aperture Diameter

Figure 4-2 shows the effect variations in accelerator aperture diameter ratio $\frac{d_a}{d_s}$ have on ion-optical performance. An intermediate grid separation ratio ($\frac{\ell_g}{d_s} = 0.494$) is used, with the other geometrical grid parameters unchanged from Figure 4-1A. The limit of obtainable normalized perveance per hole increaes significantly as accelerator

---

[*] It is important to realize that constant normalized perveance does not mean constant current. If the total accelerating voltage V_t is held constant, the beam current will increase as the grid separation ratio ℓ_g/d_s is decreased [Equation 1-5].
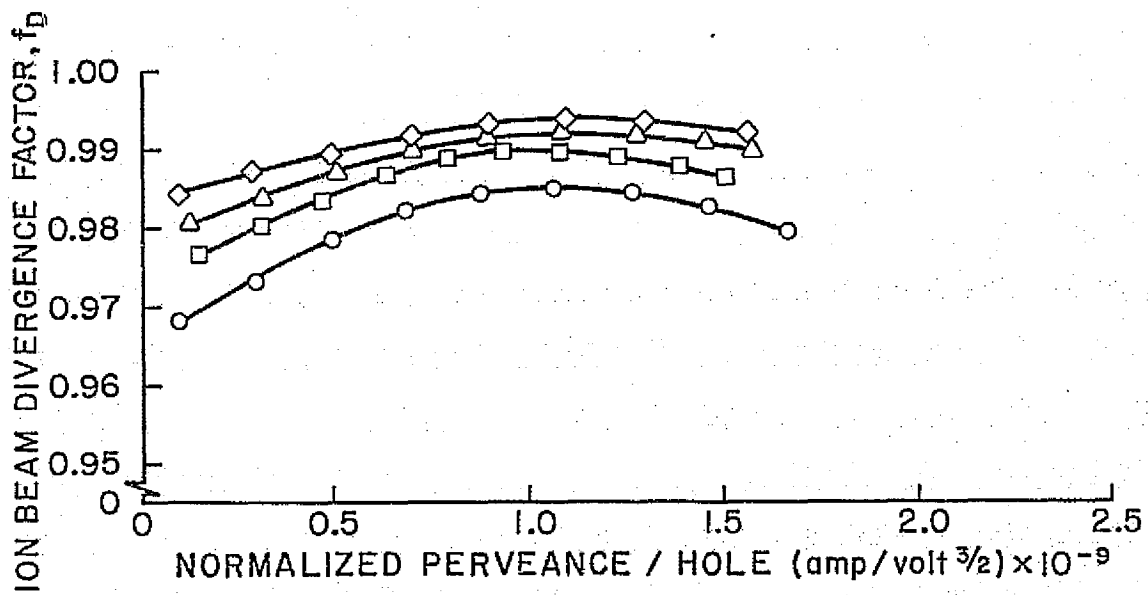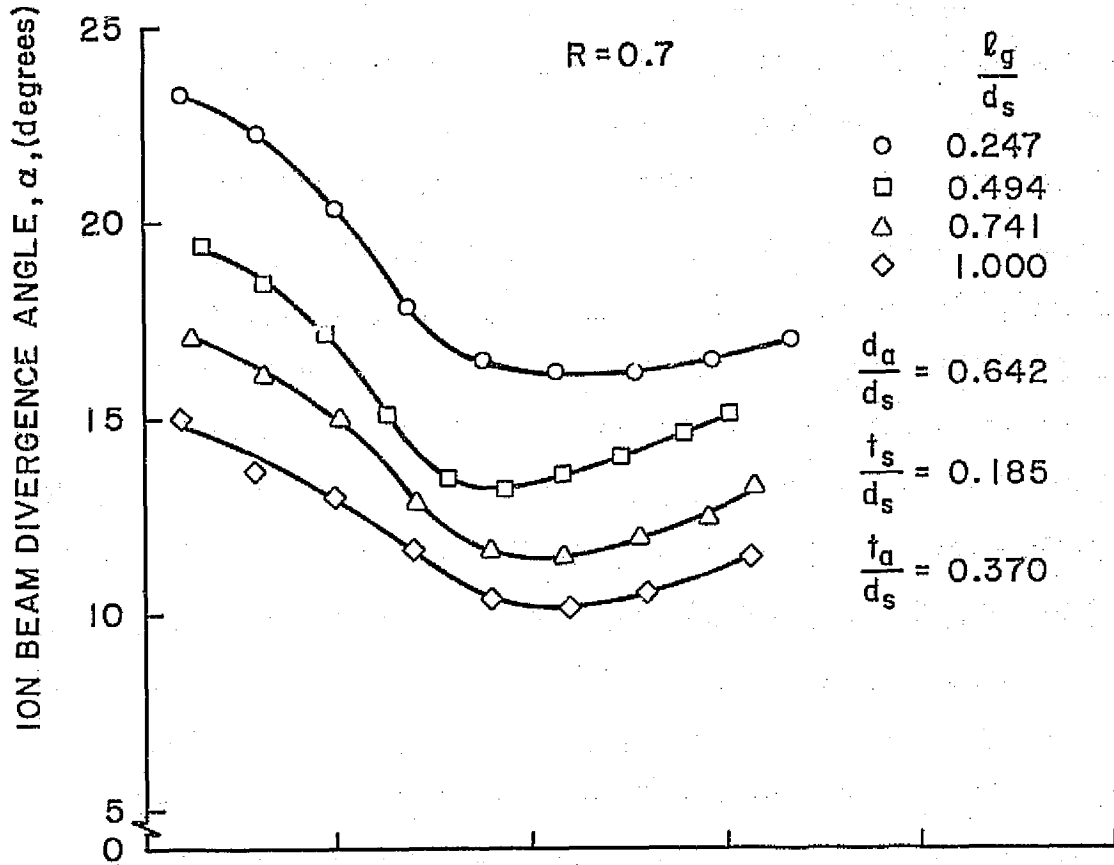
EFFECT OF GRID SEPARATION DISTANCE ON
ION BEAM DIVERGENCE

FIGURE 4-1A
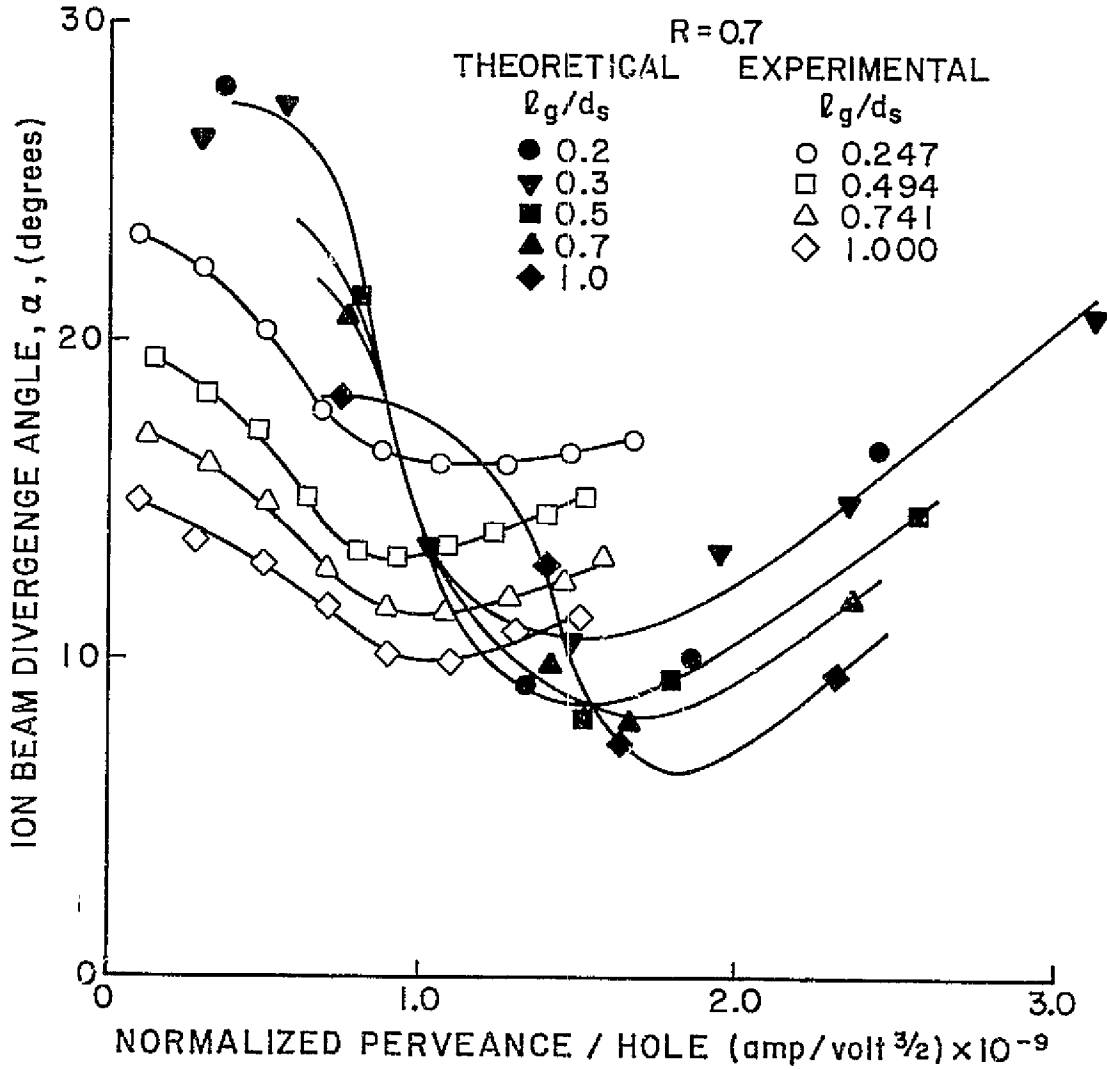
COMPARISON OF EXPERIMENTAL AND THEORETICAL RESULTS
FOR GRID SEPARATION DISTANCE VARIATION

FIGURE 4-1B
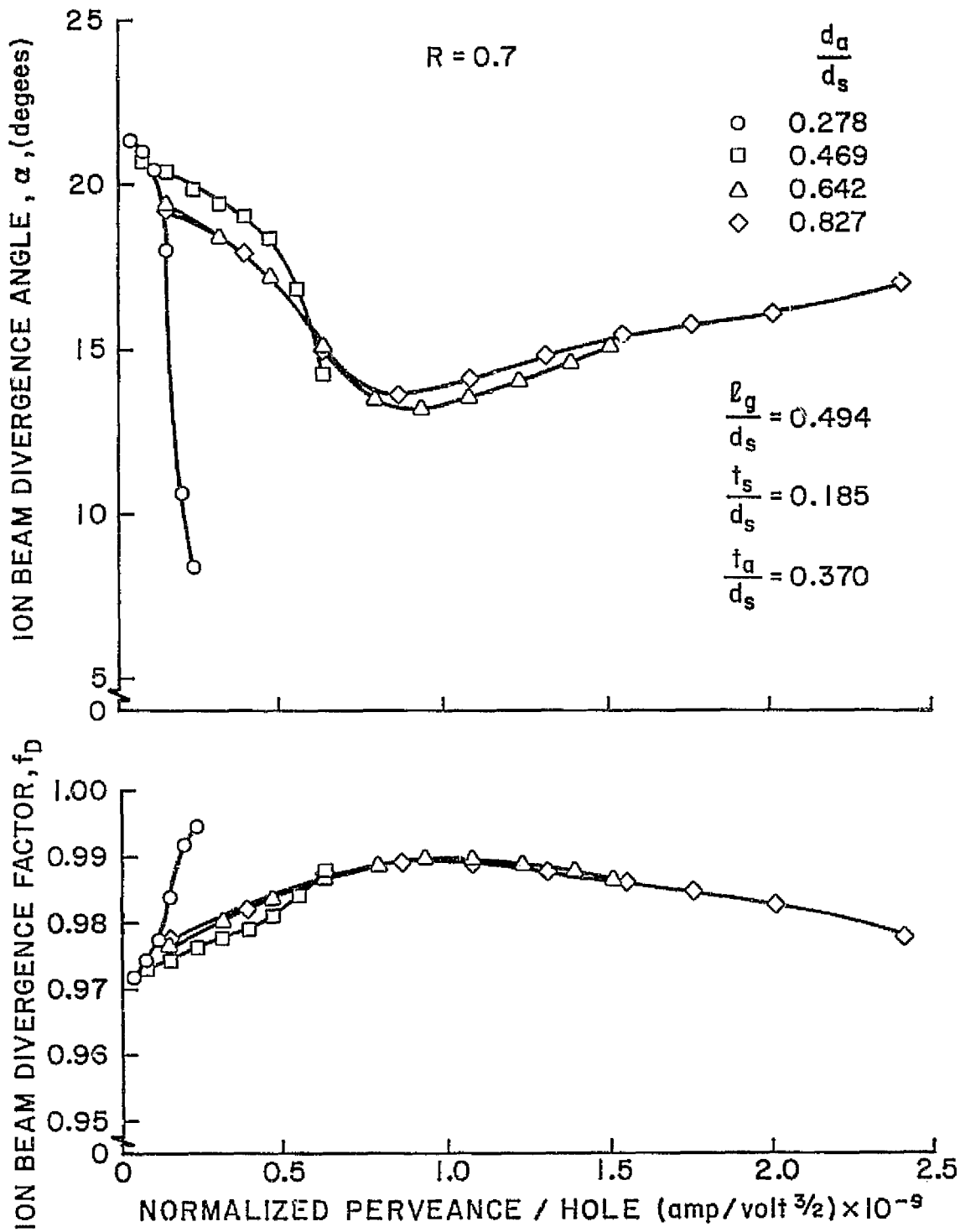
EFFECT OF ACCELERATOR APERTURE DIAMETER ON
ION BEAM DIVERGENCE

FIGURE 4-2

aperture diameter ratio increases. For values of $\frac{d_a}{d_s}$ above about

0.5 the beam divergence angles and beam divergence factors are inde-

pendent of accelerator aperture size. However, for values of $\frac{d_a}{d_s}$

below 0.5 the beam divergence angles and beam divergence factors are

dependent on accelerator aperture size. This indicates ion beamlet

focusing becomes a function of the accelerator diameter ratio if $\frac{d_a}{d_s}$

is less than about 0.5.

(c) Effect of Screen Grid Thickness

Figure 4-3 shows the effect variations in screen grid thickness

ratio $\frac{t_s}{d_s}$ have on ion-optical performance. These data used an inter-

mediate accelerator aperture diameter ratio ($\frac{d_a}{d_s} = 0.642$) with the

intermediate grid separation ratio of Figure 4-2 and the intermediate

accelerator grid thickness ratio of Figure 4-1A. Reducing the screen

grid thickness ratio from 0.2 to 0.1 tends to slightly increase the

normalized perveance per hole limit, however, a further reduction has

no significant effect on this quantity. As the screen grid thickness

ratio decreases below 0.2, the minimum beam divergence angle and maxi-

mum beam divergence factor are moved to slightly higher values of nor-

malized perveance per hole. This trend is accompanied by a reduction

in ion-optical performance in the lower ranges of normalized perveance

per hole. Overall, there is only a minor effect on ion-optical

performance caused by varying the screen grid thickness ratio.

It is postulated that different screen grid thickness ratios cause

variations in position and shape of the plasma sheath at the entrance

to each screen aperture. These variations are thought to be the main

cause of the small differences in the data.
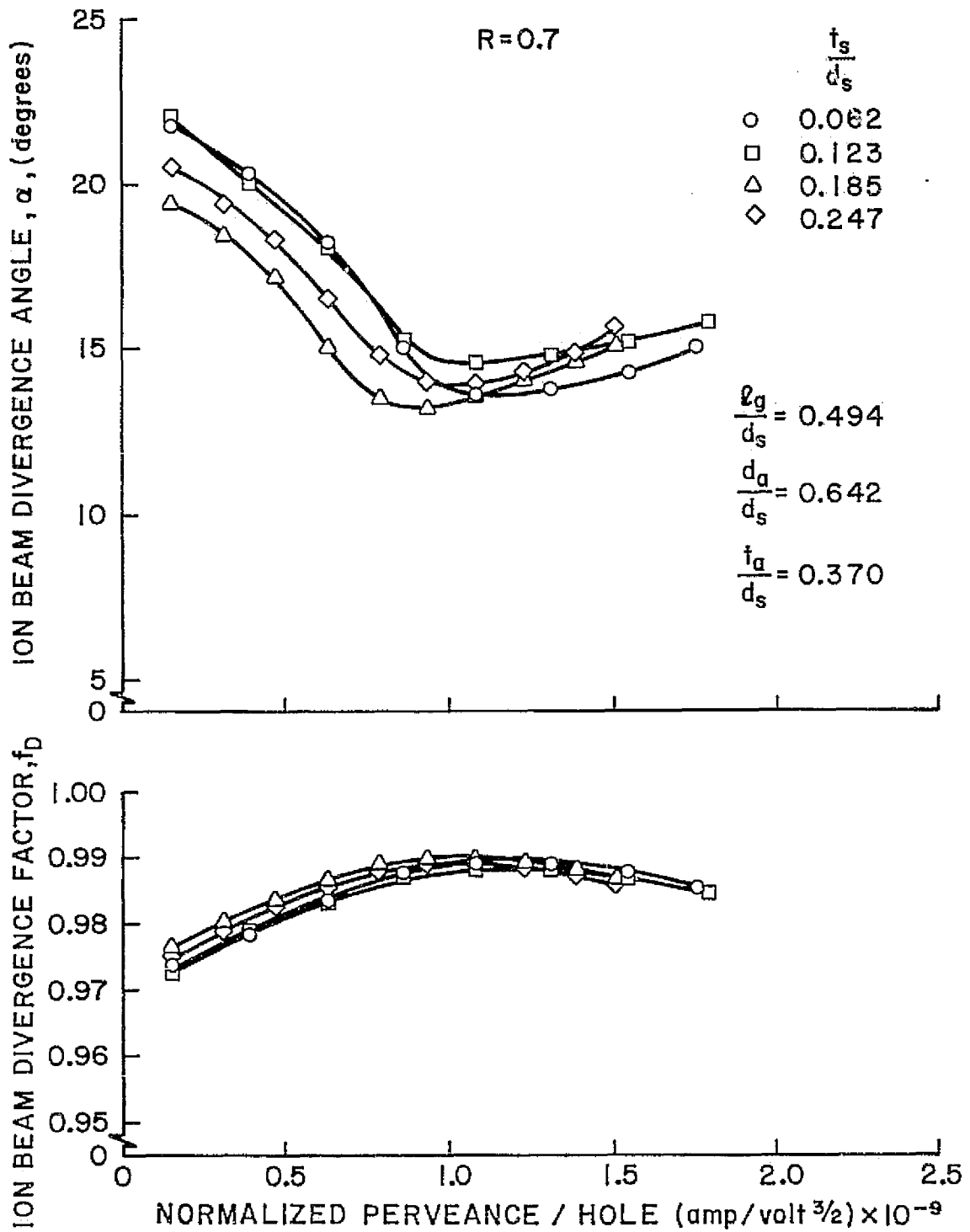
EFFECT OF SCREEN GRID THICKNESS ON
ION BEAM DIVERGENCE

FIGURE 4-3

(d) <u>Effect of Accelerator Grid Thickness</u>

Figure 4-4 shows the effect variations in accelerator grid thickness ratio $\frac{t_a}{d_s}$ have on ion-optical performance. For these data, an intermediate screen grid thickness ratio ($\frac{t_s}{d_s}$ = 0.185) is used, with the intermediate grid separation ratio of Figure 4-2 and the intermediate accelerator diameter ratio of Figure 4-3. Increasing the accelerator grid thickness ratio increases the beam divergence angle and decreases both the beam divergence factor and the limit of obtainable normalized perveance per hole. However, these degradations are fairly uniform and relatively small in magnitude.

The results shown in Figures 4-1 through 4-4 indicate that each geometrical grid parameter has a significantly independent effect on ion-optical performance. These effects can be summarized as follows.

(i) Changes in the grid separation ratio $\frac{\ell_g}{d_s}$ primarily effect the ion beam divergence angle α and the ion beam divergence factor f_D.

(ii) Varying the accelerator aperture diameter ratio $\frac{d_a}{d_s}$ above about 0.5 primarily affects the limit to the obtainable normalized perveance per hole.

(iii) Reducing the screen grid thickness ratio $\frac{t_s}{d_s}$ below about 0.2, primarily moves the minimum beam divergence angle and maximum beam divergence factor to slightly higher values of normalized perveance per hole.

(iv) Increasing the accelerator thickness ratio $\frac{t_a}{d_s}$ uniformly degrades the ion-optical performance of a particular grid set, but to a minor extent.
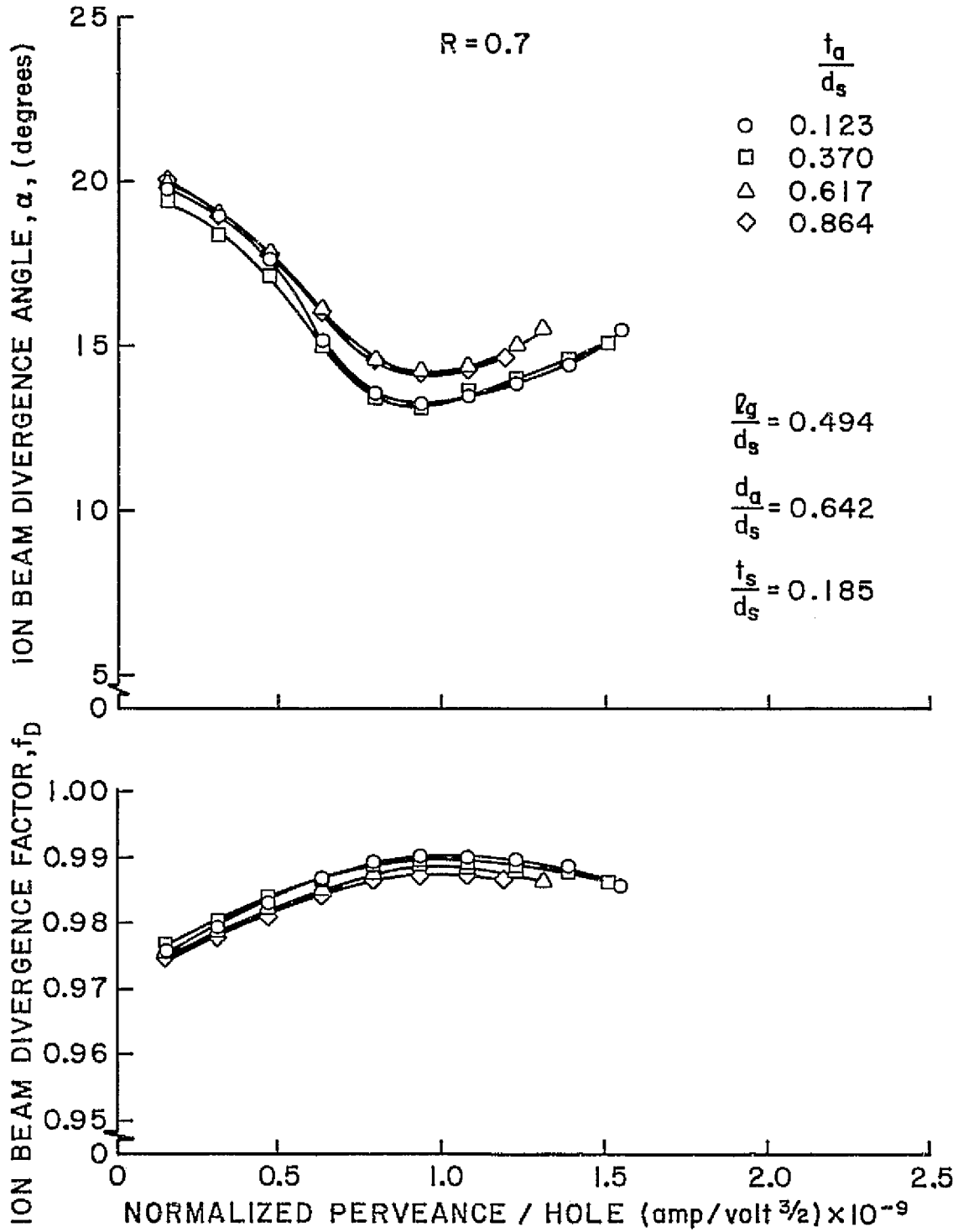
EFFECT OF ACCELERATOR GRID THICKNESS ON
ION BEAM DIVERGENCE

FIGURE 4-4

Variations in Grid Operating Conditions

To investigate the changes in ion-optical performance for various accelerating voltages, selected grid set geometries were operated at net-to-total accelerating voltage ratios ($R = \frac{V_{net}}{V_{tot}}$) of 0.5, 0.7 and 0.9. Figure 4-5 shows the effect of varying R on a "standard geometry" grid set (this designation is used because the geometrical grid parameters of Figure 4-5 are similar to those currently being investigated on developmental ion thrusters). Increasing the net-to-total accelerating voltage ratio results in a large decrease in beam divergence angle and a large increase in beam divergence factor. Figures 4-6 and 4-7 show that these changes are less pronounced for larger grid separation ratios. As shown in Figures 4-5 through 4-7, the shape of the ion-optical performance curves is essentially unaltered by variations in the parameter R. Although the curve shapes are similar, the beam divergence increases continuously with decreasing R.

Figure 4-8 shows the effect of changes in R on the ion-optical performance of a grid set using a large accelerator aperture diameter ratio with all other parameters standard. The ion-optical performance curves are very similar to those in Figure 4-5 except that in each case they continue to higher values of normalized perveance per hole, an observation predictable from the results contained in Figure 4-2.

Figure 4-9 shows the effect of changes in R on the ion-optical performance of a grid set using a small screen grid thickness ratio with all other parameters standard. The performance curves are qualitatively similar to those in Figure 4.5. However, they have reduced ion-optical performance at low normalized perveance per hole, with minimum beam divergence angles and maximum beam divergence factors
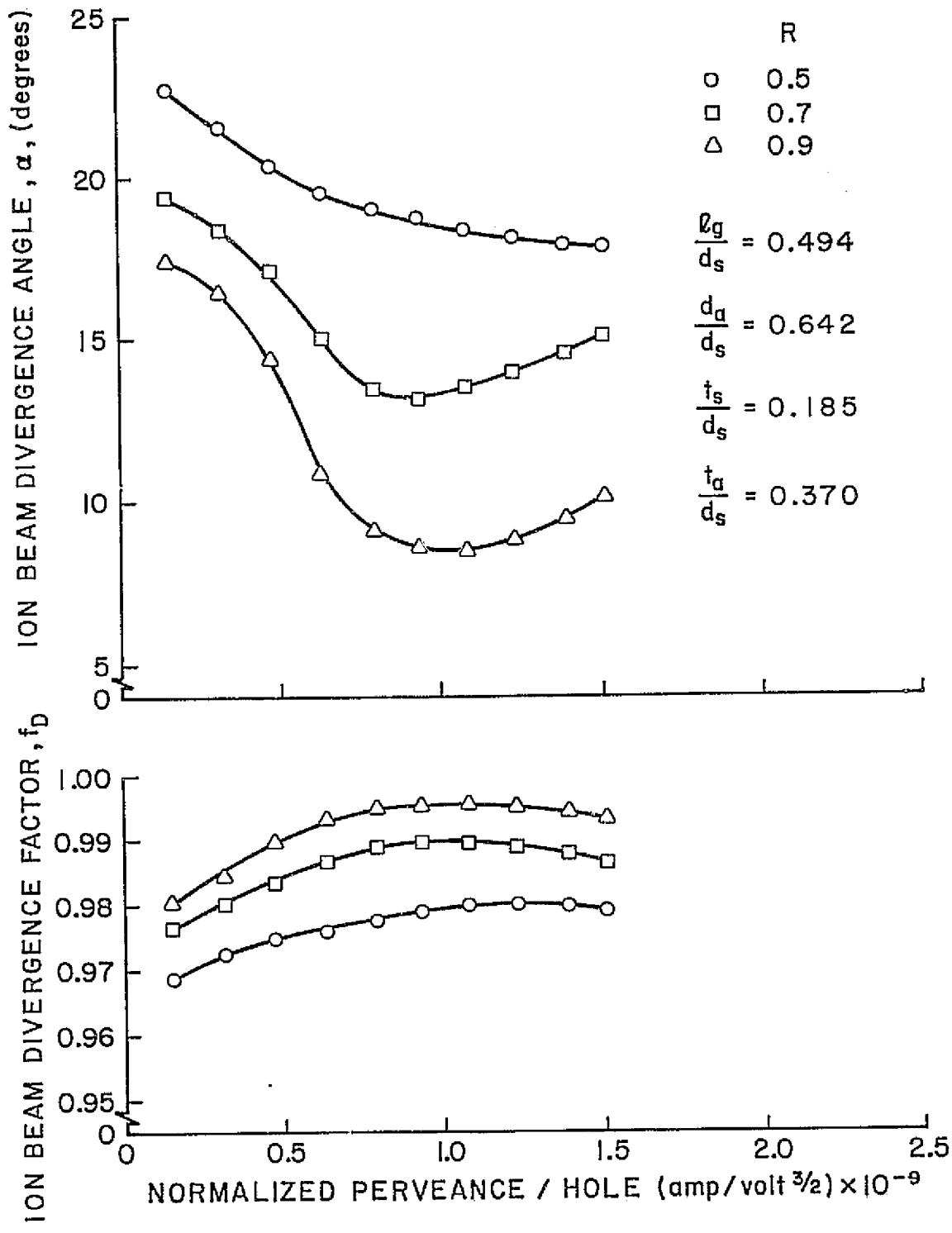
EFFECT OF R ON ION BEAM DIVERGENCE
(SMALL GRID SEPARATION DISTANCE)

FIGURE 4-5

EFFECT OF R ON ION BEAM DIVERGENCE
(MEDIUM GRID SEPARATION DISTANCE)

FIGURE 4-6
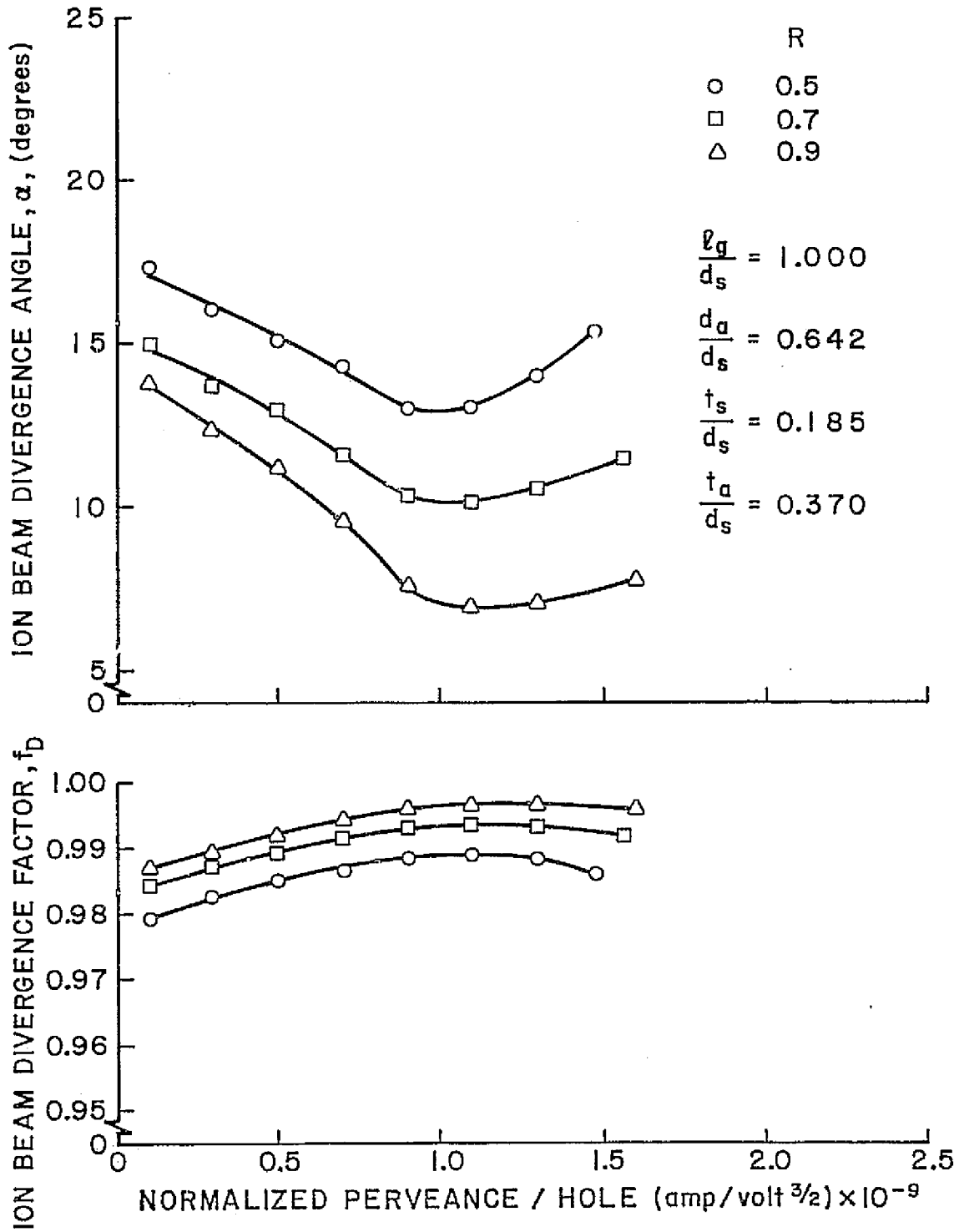
EFFECT OF R ON ION BEAM DIVERGENCE
(LARGE GRID SEPARATION DISTANCE)

FIGURE 4-7
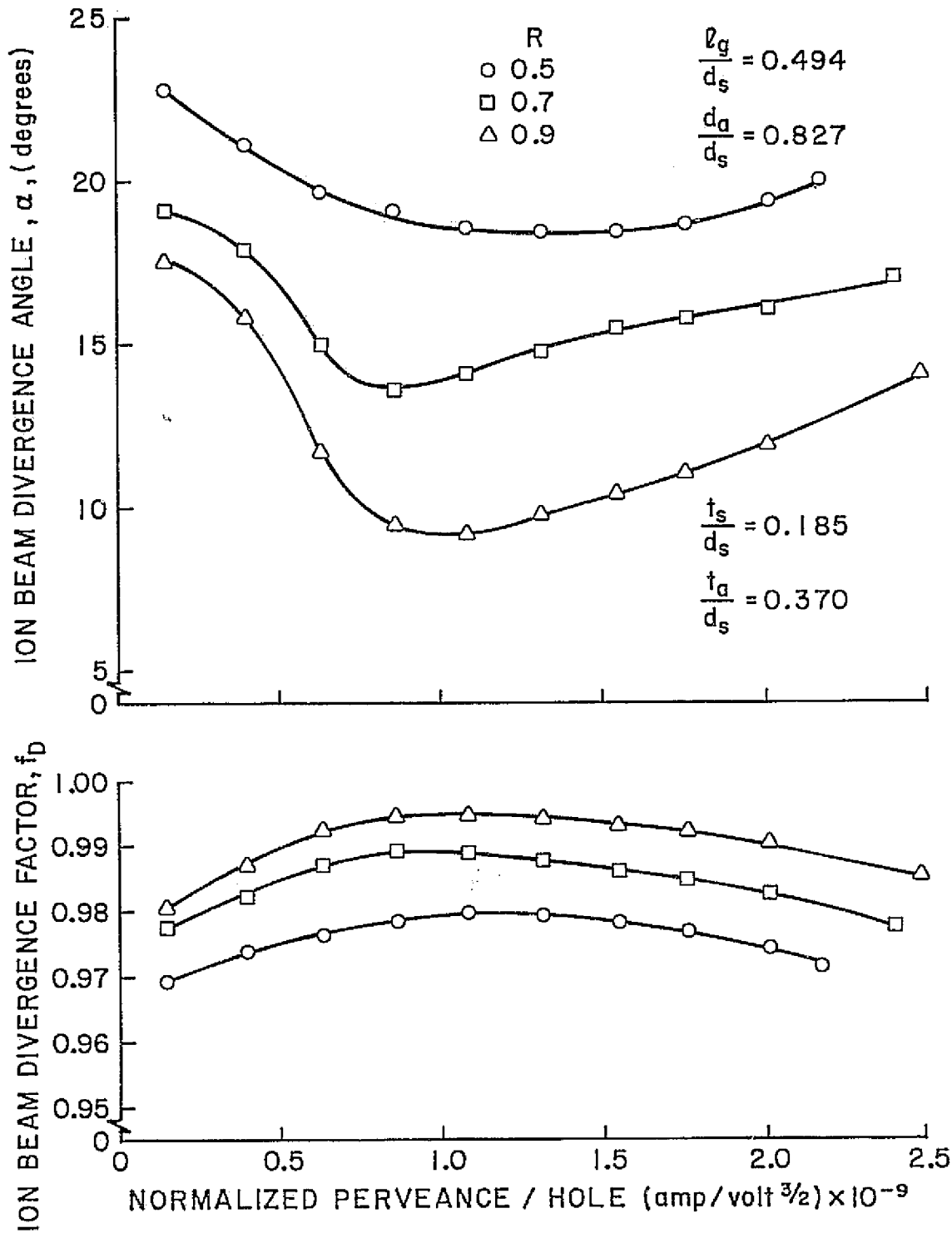
EFFECT OF R ON ION BEAM DIVERGENCE
(LARGE ACCELERATOR APERTURE DIAMETER)

FIGURE 4-8
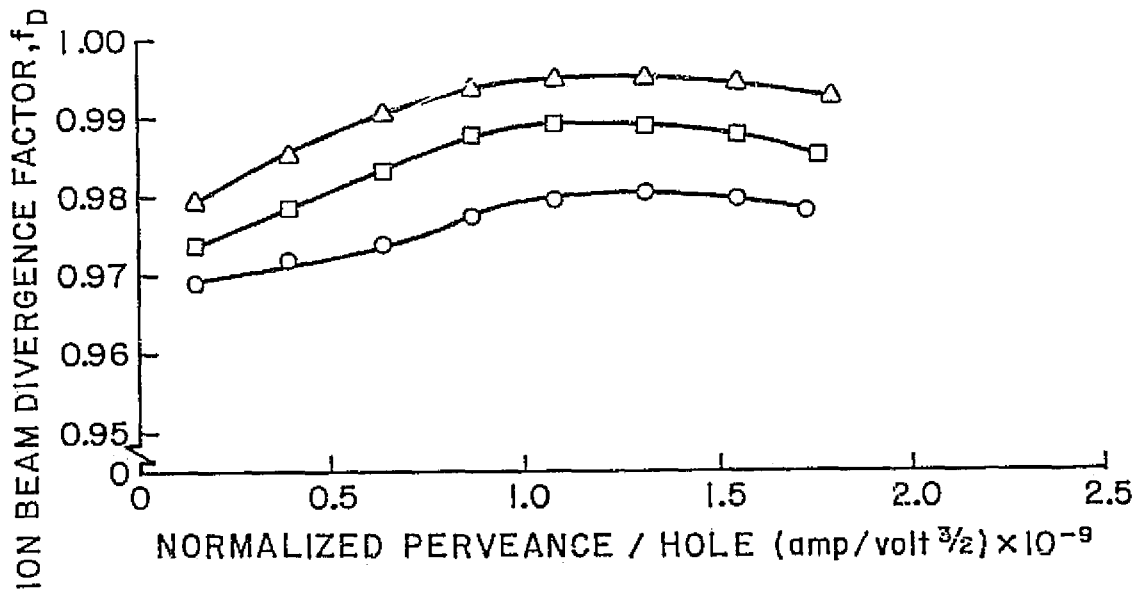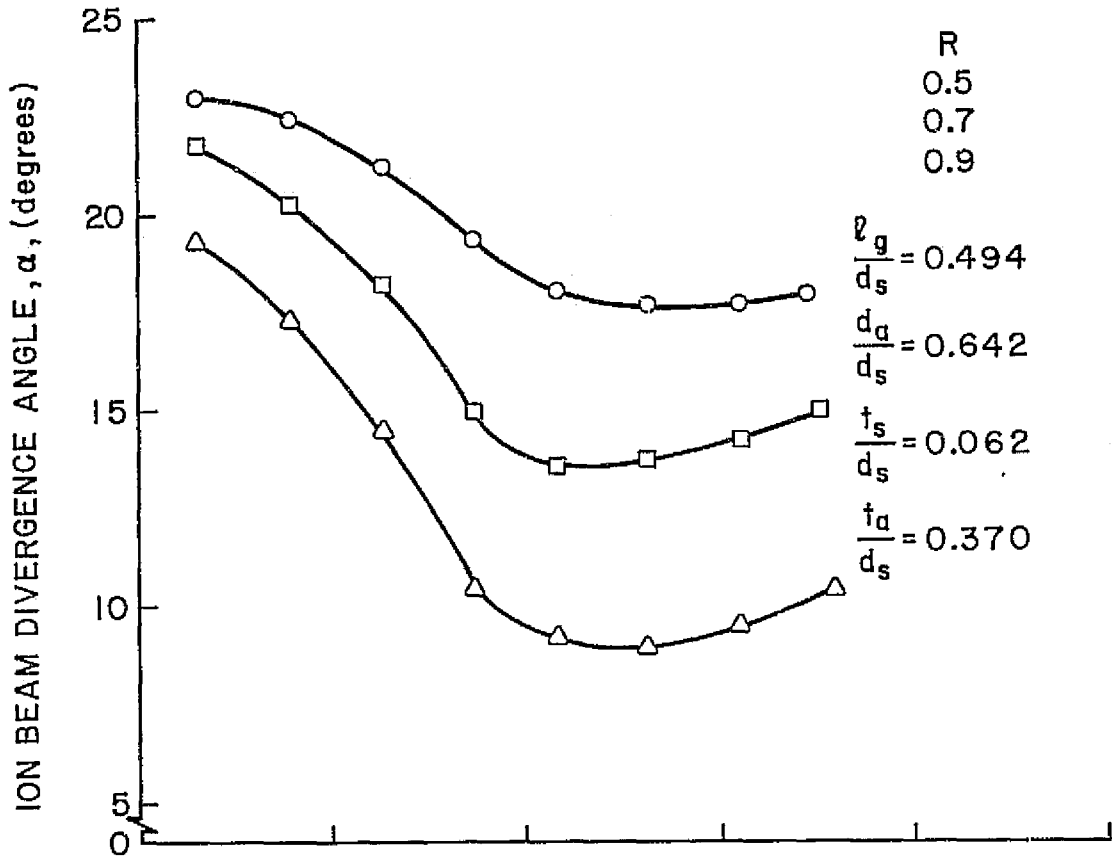
EFFECT OF R ON ION BEAM DIVERGENCE
(SMALL SCREEN GRID THICKNESS)

FIGURE 4-9

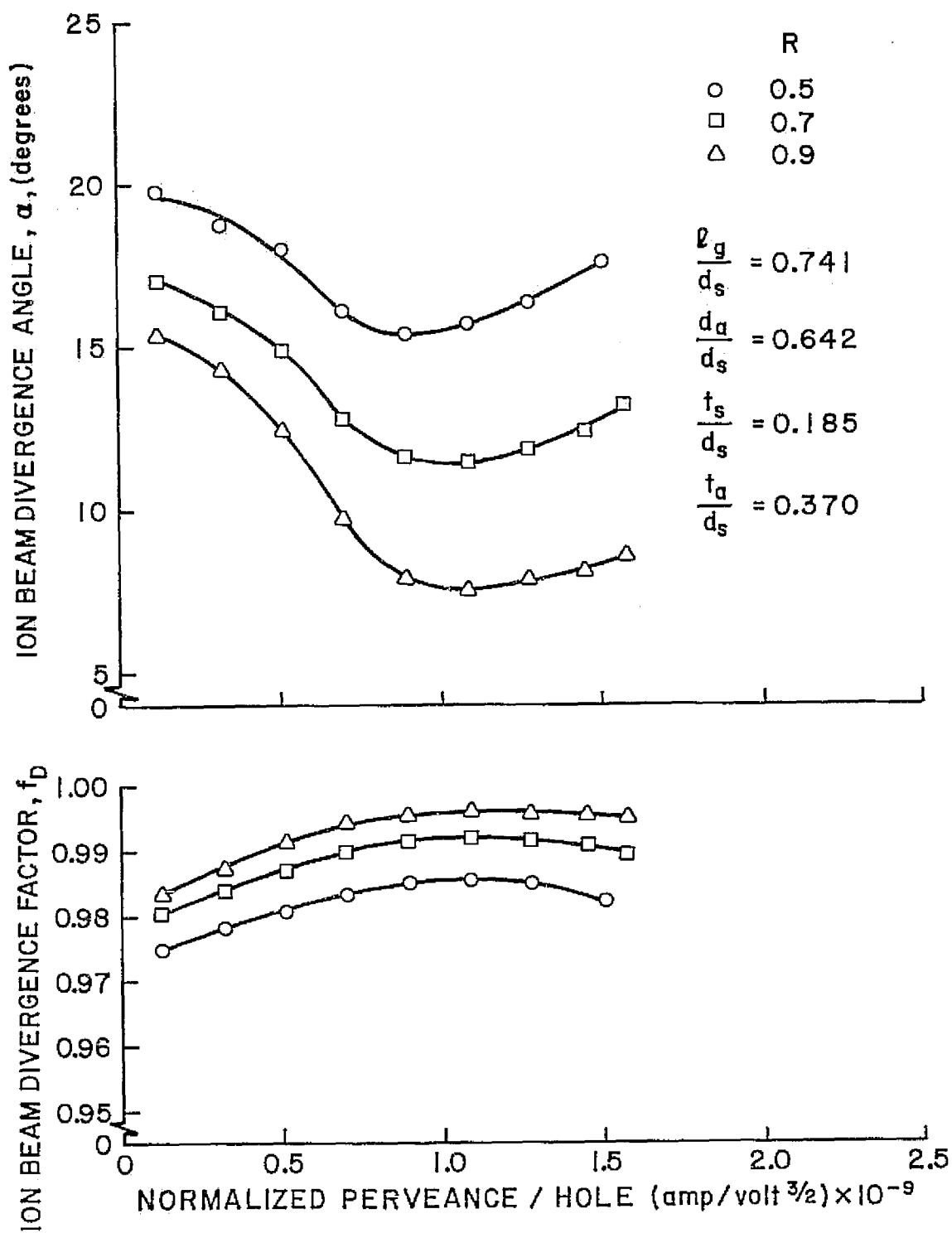occurring at slightly higher values of normalized perveance per hole. These trends are predictable from Figure 4-3.

Figure 4-10 shows the effect of changes in R on the ion-optical performance of a grid set using a large accelerator grid thickness ratio with all other parameters standard. The ion-optical performance curves are similar to those in Figure 4-5 but all have been uniformly degraded in overall performance, trends predictable from Figure 4-4.

In summary, varying the net-to-total accelerating voltage ratio produces no significant changes in the shape of the ion-optical performance curves characteristic to each geometrical grid parameter [Figures 4-1A through 4-4]. However, there is a large uniform change in the magnitudes of beam divergence angle and beam divergence factor as R is varied. For all grid set geometries investigated, reducing the negative potential on the accelerator grid (by going to higher values of R) gave no indication that neutralization electrons back-streamed into the accelerator system because of reduced electrostatic repulsion forces.

Ion Beamlet Diameter

The diameter of the ion beamlet between the grid sets was investigated for its dependence on normalized perveance per hole. To do this, accelerator grid impingement current was recorded over the operating range of normalized perveance for each grid set geometry studied. Plotting impingement current against normalized perveance per hole produced a curve which was essentially linear until the start of direct ion impingement where the curve rose sharply, indicating the limit of obtainable normalized perveance per hole. The straight line portion
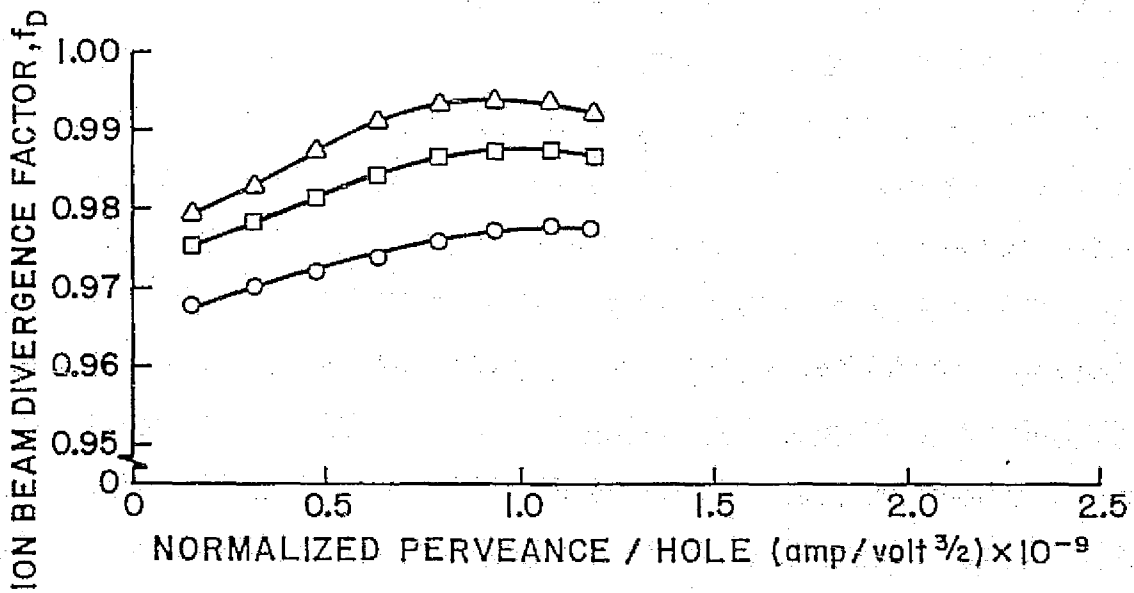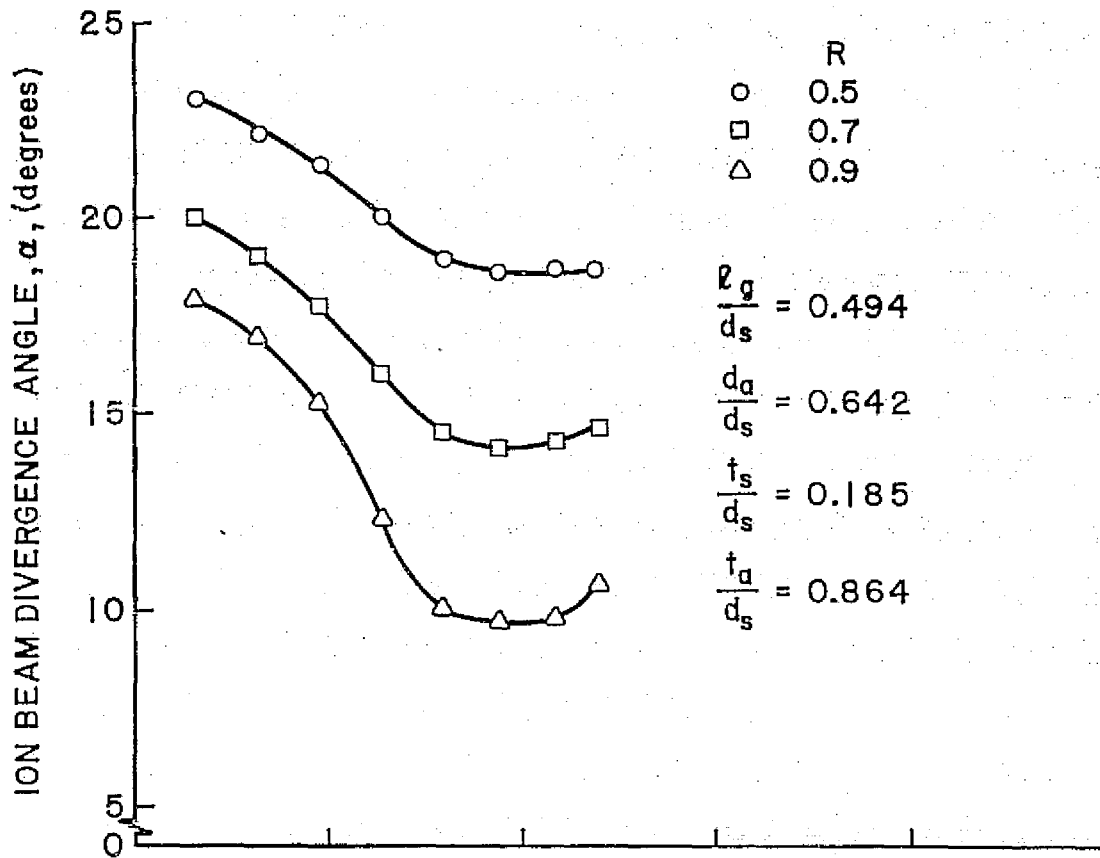
EFFECT OF R ON ION BEAM DIVERGENCE
(LARGE ACCELERATOR GRID THICKNESS)

FIGURE 4-10

was extrapolated until the actual impingement curve departed from the extrapolation by an amount equal to one hundred percent of the current indicated by the extrapolated line (a curve deviation of fifty percent was also investigated, however, the results obtained were not significantly different from those using a one hundred percent deviation). Beamlet diameter was equated to the accelerator aperture diameter at this normalized perveance per hole condition.

Figure 4-11 shows the effect of normalized perveance per hole on the ion beamlet diameter ratio $\frac{d_b}{d_s}$ for different grid separations and net-to-total accelerating voltage ratios. Increasing the grid separation ratio $\frac{\ell_g}{d_s}$ decreases the ion beamlet diameter ratio $\frac{d_b}{d_s}$ slightly for the same value of normalized perveance per hole. Decreases in beamlet diameter ratio for constant normalized perveance per hole were also observed as the net-to-total accelerating voltage ratio was increased from 0.5 to 0.9. These changes were not as significant as those obtained by varying the grid separation ratio. The experimental results in Figure 4-11 have been compared to similar data obtained theoretically by Kaufman [5]. Kaufman's results agree qualitatively with experimental trends, but the quantitative agreement is poor.

Application to Design

Grid sets may be designed to produce specified ion-optical performance by using the results contained in Figures 4-1A through 4-10. These graphical results show, that to a good approximation, complete independence may be assumed to exist between the effect each geometrical grid parameter has on ion-optical performance. For example, magnitudes of beam divergence angle and beam divergence factor can be
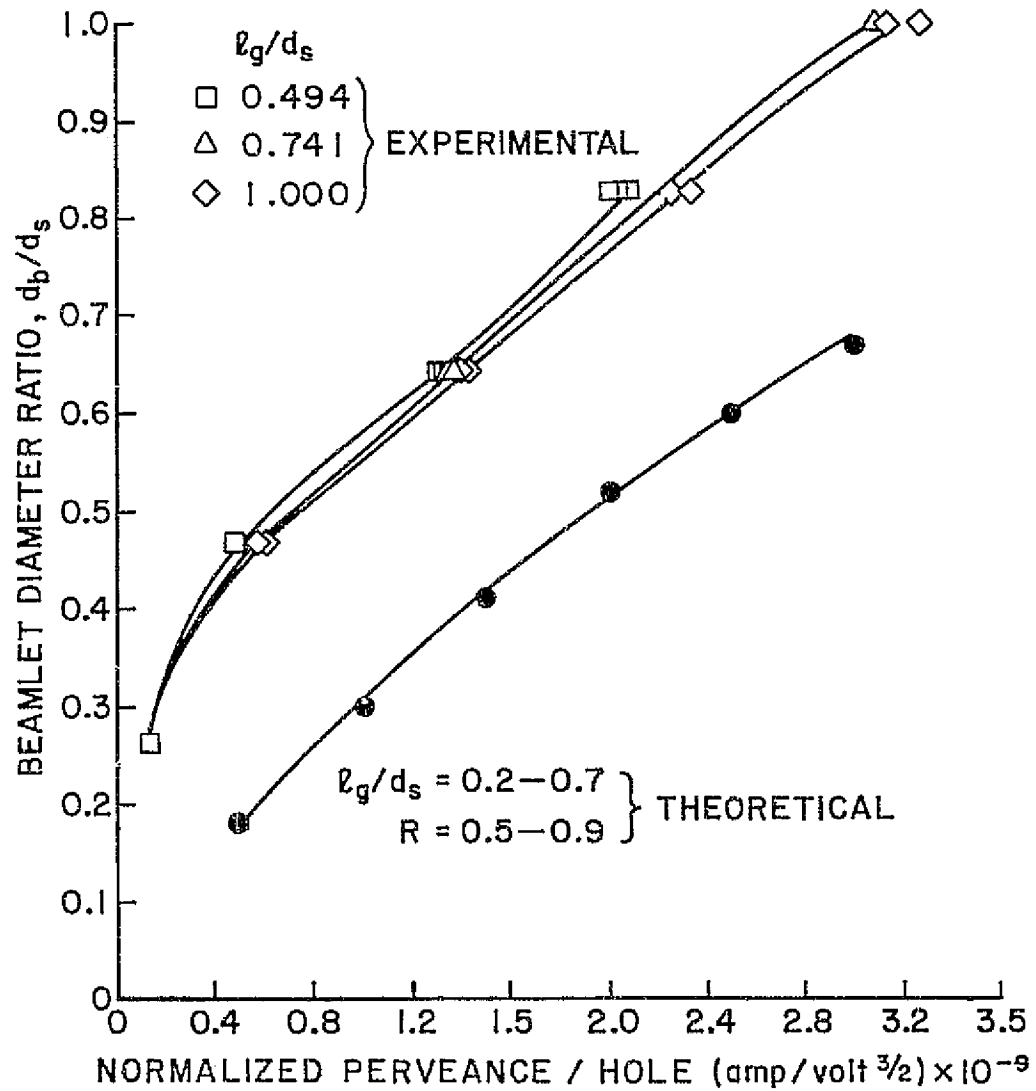
BEAMLET DIAMETER AS A FUNCTION OF
NORMALIZED PERVEANCE PER HOLE

FIGURE 4-11

assumed to depend solely on the grid separation ratio $\frac{\ell_g}{d_s}$ and the net-to-total accelerating voltage ratio R. Similarly, the limit of obtainable normalized perveance per hole can be determined by assuming it depends only on the accelerator aperture diameter ratio $\frac{d_a}{d_s}$, while the normalized perveance per hole at which the minimum beam divergence angle and maximum beam divergence factor occur can be determined (for a small range of normalized perveance per hole about a value of 1.0 x 10^{-9} amp/volt$^{3/2}$) by assuming it depends only on the screen grid thickness ratio $\frac{t_s}{d_s}$.

Figures 4-12 and 4-13 show four grid sets which were designed to give good ion-optical performance over different ranges of normalized perveance. The magnitudes of the beam divergence angles and beam divergence factors were predicted from Figure 4-7, the limit to the obtainable normalized perveance was predicted from Figure 4-2 and the normalized perveance at which the minimum beam divergence angle and maximum beam divergence factor occurred was predicted from Figure 4-3. Table 2 compares these predicted results with those actually measured from Figures 4-12[*] and 4-13. Good agreement between these results is shown, indicating the validity of assuming complete independence between the effect each geometrical grid parameter has on ion-optical performance.

The low and middle normalized perveance designs shown in Figure 4-12 represent grid sets embodying the "Small Hole Accelerator

---

[*] No table of predicted performance appears for the "middle normalized perveance design" since these data are identical to that previously shown in Figure 4-7.

Grid" concept used to reduce the accelerator grid open area fraction and hence un-ionized propellant loss. This in turn improves ion source efficiency [14].

Table 2. COMPARISON OF PREDICTED AND

EXPERIMENTAL ION-OPTICAL PERFORMANCE

(a) Low Normalized Perveance Design

$$\frac{\ell_g}{d_s} = 1.000, \ \frac{d_a}{d_s} = 0.469, \ \frac{t_s}{d_s} = 0.185, \ \frac{t_a}{d_s} = 0.370$$

Nomenclature

$\alpha_{min.}$ = minimum ion beam divergence angle (degrees).

$N \cdot P(\alpha_{min.})$ = normalized perveance at $\alpha_{min.}$ (amp/volt$^{3/2}$).

$f_D max.$ = maximum ion beam divergence factor.

$N \cdot P(f_D max.)$ = normalized perveance at $f_D max.$

$N \cdot P_{max.}$ = limit to the obtainable normalized perveance.

$\alpha(N \cdot P_{max.})$ = beam divergence angle at $N \cdot P_{max.}$.

$f_D(N \cdot P_{max.})$ = beam divergence factor at $N \cdot P_{max.}$.

| | R = 0.7 | | R = 0.9 | |
	Predicted Result	Measured Result	Predicted Result	Measured Result
$\alpha_{min.}$	10.1	8.9	6.9	6.6
$N \cdot P(\alpha_{min.})$	0.63×10^{-9}	0.80×10^{-9}	0.63×10^{-9}	0.80×10^{-9}
$f_D max.$	0.9935	0.9943	0.9965	0.9963
$N \cdot P(f_D max.)$	0.63×10^{-9}	0.80×10^{-9}	0.63×10^{-9}	0.80×10^{-9}
$N \cdot P_{max.}$	0.63×10^{-9}	0.80×10^{-9}	0.63×10^{-9}	0.80×10^{-9}
$\alpha(N \cdot P_{max.})$	10.1	8.9	6.9	6.6
$f_D(N \cdot P_{max.})$	0.9935	0.9943	0.9965	0.9963

(b) High Normalized Perveance Design

$$\frac{\ell_g}{d_s} = 1.000, \quad \frac{d_a}{d_s} = 0.827, \quad \frac{t_s}{d_s} = 0.123, \quad \frac{t_a}{d_s} = 0.370$$

	R = 0.7		R = 0.9	
	Predicted Result	Measured Result	Predicted Result	Measured Result
$\alpha_{min.}$	10.1	10.6	6.9	7.5
$N \cdot P(\alpha_{min.})$	1.10×10^{-9}	1.20×10^{-9}	1.10×10^{-9}	1.20×10^{-9}
$f_D max.$	0.9935	0.9931	0.9965	0.9960
$N \cdot P(f_D max.)$	1.20×10^{-9}	1.30×10^{-9}	1.20×10^{-9}	1.20×10^{-9}
$N \cdot P_{max.}$	2.40×10^{-9}	2.46×10^{-9}	2.62×10^{-9}	2.62×10^{-9}
$\alpha(N \cdot P_{max.})$	13.3	14.8	9.8	10.7
$f_D(N \cdot P_{max.})$	0.9840	0.9864	0.9925	0.9916

(c) Very High Normalized Perveance Design

$$\frac{\ell_g}{d_s} = 1.000, \quad \frac{d_a}{d_s} = 1.000, \quad \frac{t_s}{d_s} = 0.062, \quad \frac{t_a}{d_s} = 0.370$$

	R = 0.7		R = 0.9	
	Predicted Result	Measured Result	Predicted Result	Measured Result
$\alpha_{min.}$	10.1	10.6	6.9	7.2
$N \cdot P(\alpha_{min.})$	1.15×10^{-9}	1.20×10^{-9}	1.15×10^{-9}	1.30×10^{-9}
$f_D max.$	0.9935	0.9931	0.9965	0.9963
$N \cdot P(f_D max.)$	1.20×10^{-9}	1.30×10^{-9}	1.20×10^{-9}	1.30×10^{-9}
$N \cdot P_{max.}$	3.30×10^{-9}	3.47×10^{-9}	3.30×10^{-9}	3.55×10^{-9}
$\alpha(N \cdot P_{max.})$	15.3	16.8	13.7	13.2
$f_D(N \cdot P_{max.})$	0.9780	0.9787	0.9865	0.9869
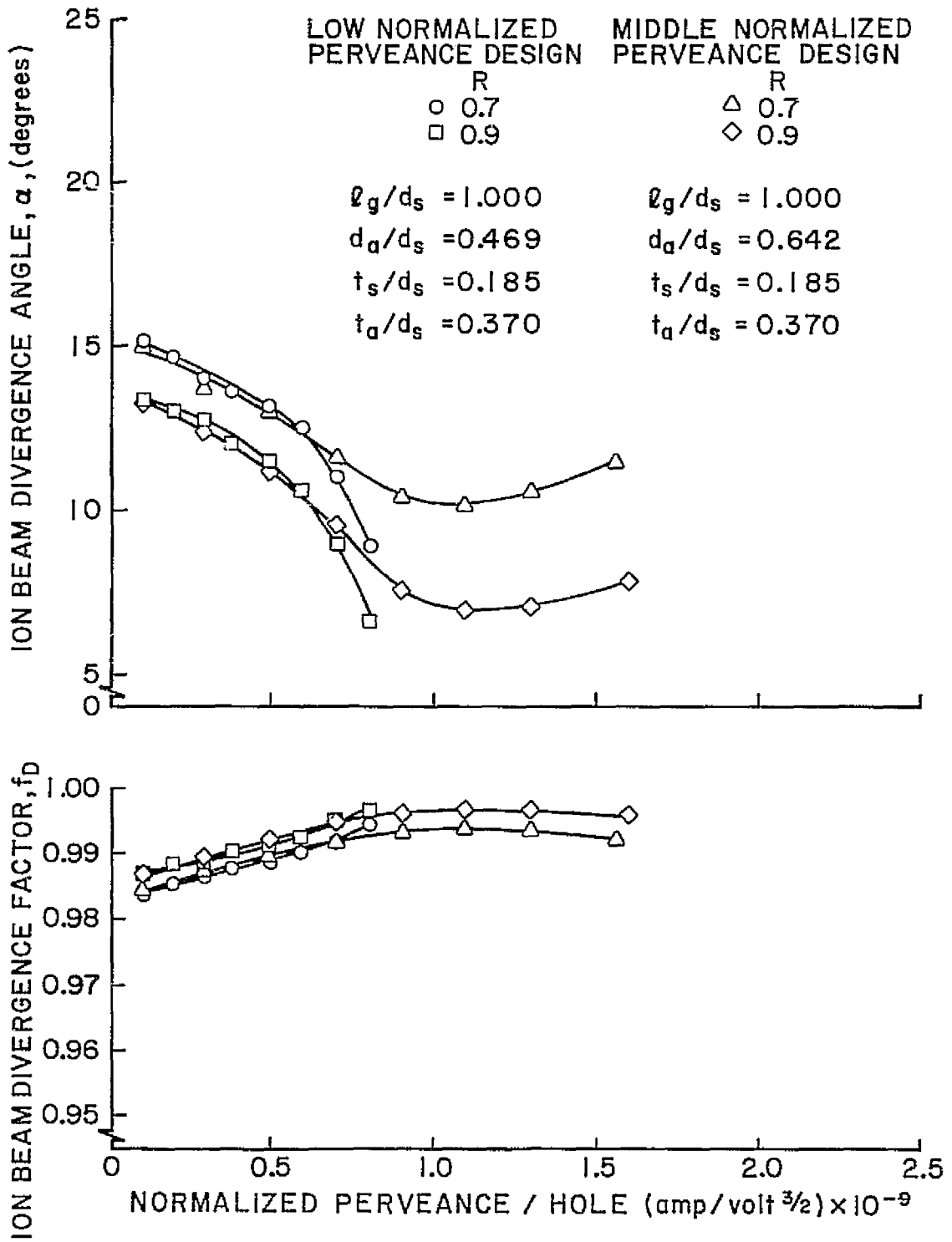
LOW AND MIDDLE NORMALIZED PERVEANCE
GRID SET DESIGNS

FIGURE 4-12
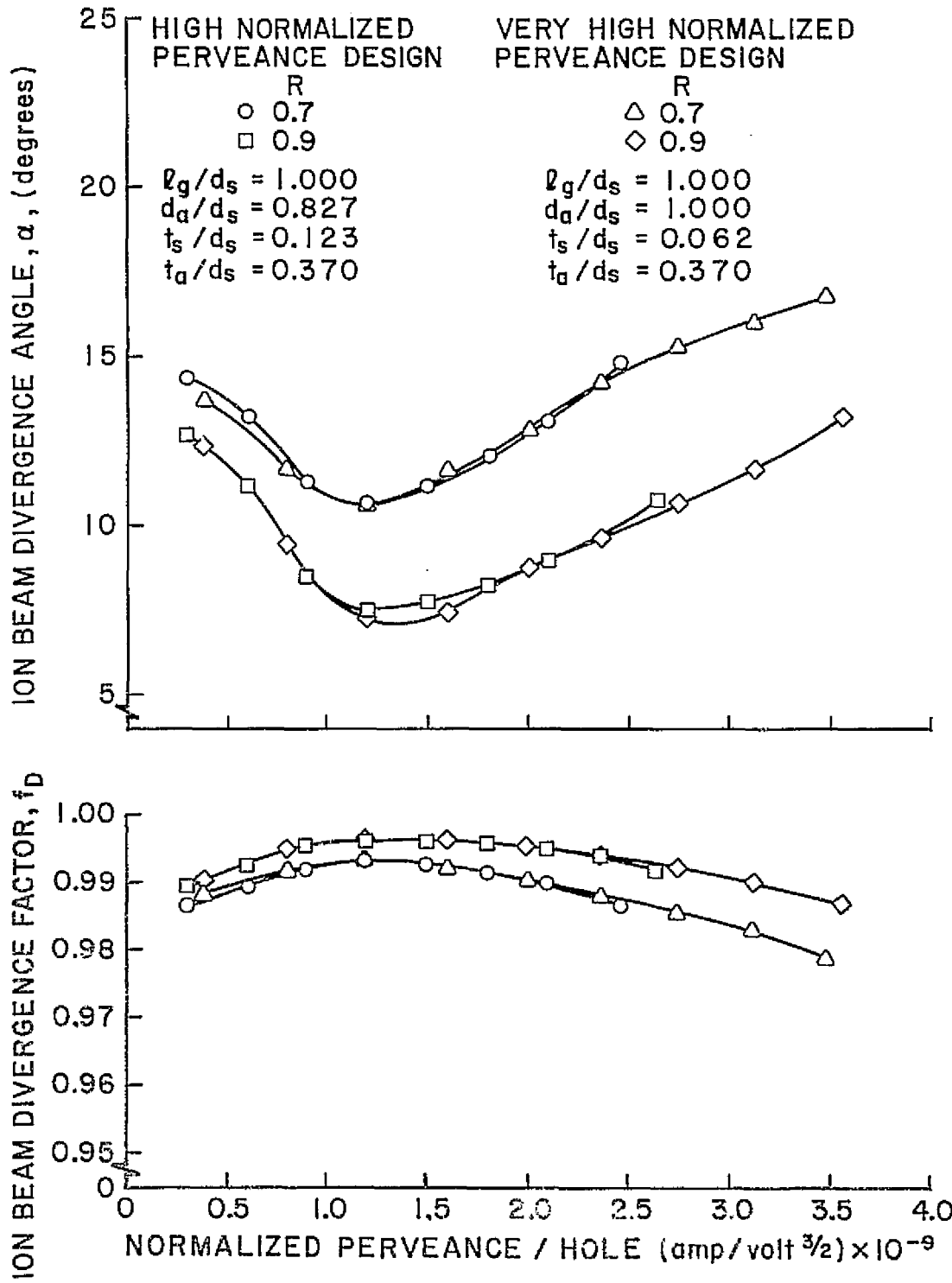
HIGH AND VERY HIGH NORMALIZED PERVEANCE
GRID SET DESIGNS

FIGURE 4-13

Figure 4-13 shows two grid sets designed to operate at increased levels of normalized perveance per hole. The high normalized perveance design is considered more practical of the two. It uses a smaller accelerator aperture diameter ratio ($\frac{d_a}{d_s} = 0.827$ compared to $\frac{d_a}{d_s} = 1.000$) for some reduction of un-ionized propellant loss, while employing a sufficiently thick screen grid to yield an acceptable ion sputter erosion lifetime. The very high normalized perveance grid set design illustrates the experimental limit to ion-optical performance. A beam divergence factor greater than 0.99 is evident for a normalized perveance of 0.4 to 3.1 x 10^{-9} amp/volt$^{3/2}$ with a net-to-total accelerating voltage ratio of 0.9. The significant increase beyond the theoretical Childs' law normalized perveance limit for mercury, 3.03 x 10^{-9} amp/volt$^{3/2}$, indicates the approximate nature of a one-dimensional derivation when used for a two-dimensional configuration at these high operating conditions.

Chapter 5

A DESIGN EXAMPLE

A Method of Predicting Ion-Optical Performance

A technique is described to predict ion-optical performance for developmental electron-bombardment thrusters. The technique makes extensive use of the graphical results presented in Chapter 4. The data presented herein were obtained from a plasma uniformly dense across the ion extraction area and thus cannot be applied directly to full sized ion thrusters, where the plasma density within the discharge chamber is significantly non-uniform across the screen grid area. Incorporating the effects of plasma non-uniformity into calculations of ion-optical performance requires a knowledge of the plasma (and hence ion) density profile. Once this profile is obtained, the graphical data can be used to determine ion-optical performance by partitioning the surface of a full sized grid set into regions of near uniform ion density. The ion-optical performance is then determined for each individual region. Averaging these results determines the ion-optical performance for the entire grid set.

To illustrate this method, the 30-cm diameter Engineering Model electron-bombardment ion thruster, currently being developed as a primary propulsion source for extended space missions [15], is analyzed to predict its ion-optical performance. The non-dimensionalized grid set parameters for this thruster are as follows:

$$\frac{\ell_g}{d_s} = 0.37$$

$$\frac{d_a}{d_s} = 0.80$$

$$\frac{t_s}{d_s} = 0.20$$

$$\frac{t_a}{d_s} = 0.27$$

Developmental ion thrusters employ spherically dished grid sets to reduce changes in grid separation distance caused by thermal distortion [16]. However, ion beam divergence is increased when the grid sets are dished. This effect is compensated for by using a slightly different screen and accelerator aperture array [16], the ion beam divergence from a compensated dished grid set then closely approximates the ion beam divergence from a flat grid set. Hence, the results contained in Chapter 4 using a flat grid set geometry are also valid for compensated dished grids.

Figure 5-1 shows the ion density profile for the 30-cm E.M. ion thruster. This profile was obtained from unpublished data supplied by Hughes Research Laboratories [17] and represents variations in ion density directly adjacent to the screen grid. The dependence of profile shape on beam current was investigated and found to be an insignificant factor. The variation is therefore assumed valid for lower ranges of beam current. The ion density depicted in Figure 5-1 is for a beam current of 2.0 ampere (the designed operating level for the 30-cm E.M. ion thruster).

Calculations were performed for the 30-cm E.M. ion thruster to predict ion beam divergence factors for thruster operation at beam currents of 2.0, 1.5 and 1.0 ampere. To illustrate the method of analysis used in performing these calculations a worked example is
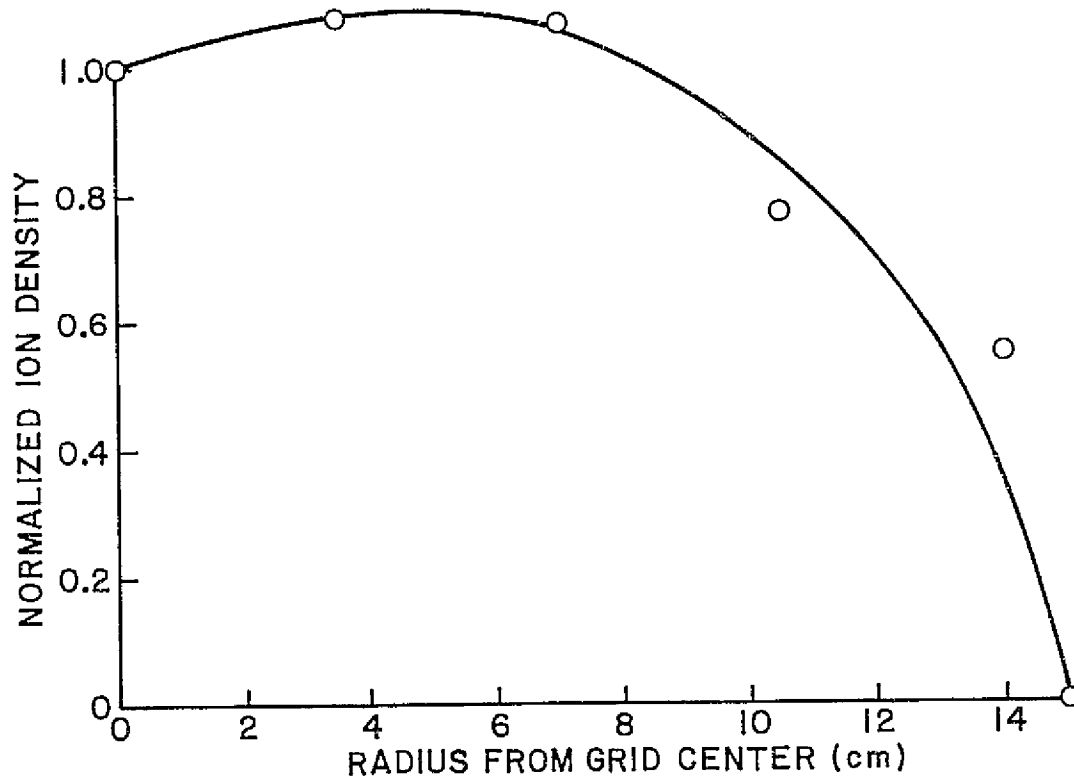
ION DENSITY PROFILE OF THE 30-cm
ENGINEERING MODEL ION THRUSTER

FIGURE 5-1

presented in step form, where the beam divergence factor is determined
for an ion beam current of 2.0 ampere.

Step I.

The 30-cm grid set is partitioned into five equal annular areas
and the average normalized ion density is determined from Figure 5-1
for each region (calculations have shown that five equal area regions
produce reliable results). Next, the fraction of total ion current
that each region can extract is calculated. This is done by summing
the normalized ion density of each region and then taking the ratio of
the normalized ion density of each region to this sum. From these
values, the ion current that must be extracted from each region to pro-
duce the desired beam current of 2.0 ampere is calculated. Table 3
shows the results obtained (region A is located at the grid center
while region E corresponds to the annular area around the grid edge).

Table 3. ION BEAM DIVERGENCE
CALCULATIONS, STEP I

Region	Normalized Ion Density	Fraction of Total Current/Region	Current/Region For a 2.0 amp. Beam
A	1.05	0.281	0.562
B	1.00	0.268	0.536
C	0.84	0.223	0.446
D	0.61	0.163	0.326
E	0.24	0.065	0.130

Step II.

The average normalized perveance per hole for each region is cal-
culated by using the equation

$$N \cdot P/H = \frac{J_R}{V_t^{3/2}} \left(\frac{\ell_e}{d_s}\right)^2 \frac{X}{Y} \tag{5-1}$$

where J_R is the ion current extracted from each region [last column of Table 3] and V_t is the total accelerating voltage (V_t = 1500 V for the 30-cm E.M. ion thruster). The quantity $\left(\frac{\ell_e}{d_s}\right)^2$ is found by substituting the ratio $\frac{\ell_g}{d_s}$ = 0.37 into Equation (2-4), this gives a value of $\left(\frac{\ell_e}{d_s}\right)^2$ = 0.39. The ratio $\frac{X}{Y}$ is the number of regions (X = 5) divided by the number of apertures in a 30-cm E.M. grid set (Y = 15173, [18]). With these substitutions, Equation (5-1) reduces to

$$N \cdot P/H = 2.21 \times 10^{-9} (J_R) \tag{5-2}$$

The average normalized perveance per hole is calculated for each region using Equation (5-2). Table 4 lists these results.

Table 4. ION BEAM DIVERGENCE CALCULATIONS, STEP II

Region	N-P/H (amp/volt$^{3/2}$)
A	1.24×10^{-9}
B	1.18×10^{-9}
C	0.99×10^{-9}
D	0.72×10^{-9}
E	0.29×10^{-9}

Step III.

The ion-optical performance expected from the 30-cm E.M. grid set geometry is approximated by interpolating an ion-optical performance curve from Figure 4-1, using the E.M. ion thruster grid separation

ratio $\frac{\ell_g}{d_s}$ = 0.37 (the E.M. ion thruster uses a net-to-total accelerating

voltage ratio of 0.7 and operates on mercury propellant). Although the

E.M. grid set geometry has slightly different values of $\frac{d_a}{d_s}$, $\frac{t_s}{d_s}$ and $\frac{t_a}{d_s}$

from the values contained in Figure 4-1, these differences produce no

significant changes in the ion beam divergence factors [Figures 4-2

through 4-4]. An ion beam divergence factor is obtained for each

region by using the normalized perveance per hole values in Table 4 to

read beam divergence factors from the interpolated ion-optical perform-

ance curve found from Figure 4-1. The results are shown in Table 5.

Table 5. ION BEAM DIVERGENCE

CALCULATIONS, STEP III

Region	Ion Beam Divergence Factor f_D
A	0.987
B	0.987
C	0.988
D	0.985
E	0.977

Step IV.

The ion beam divergence factor for the entire grid set is de-

termined by using a weighted averaging procedure. Since more current

is extracted from the center of the grid set than the edge, the value

of f_D for each region is multiplied by a "weighted fraction of total

current/region," this quantity is obtained by dividing the results in

column three of Table 3 by the fraction of total current/region in

region E. These results are then averaged in the usual manner to

give the total ion beam divergence factor. Table 6 illustrates the procedure.

Table 6. ION BEAM DIVERGENCE
CALCULATIONS, STEP IV

Region	Weighted Fraction of Total Current/Region	Weighted Beam Divergence Factor f_D	Average f_D
A	4.373	4.267	
B	4.123	4.069	$f_D = \dfrac{15.172}{15.384}$
C	3.430	3.389	
D	2.508	2.470	$f_D = 0.986$
E	1.000	0.977	
	Total = 15.384	Total = 15.172	

Similar calculations were also performed for an ion beam current of 1.5 and 1.0 ampere. Table 7 lists the results of these calculations.

Table 7. ION BEAM DIVERGENCE CALCULATIONS,
1.5 AND 1.0 AMPERE ION BEAM

Region	N·P/H (amp/volt$^{3/2}$)	f_D	Weighted f_D	Average f_D
$J_{BEAM} = 1.5A$				
A	0.93×10^{-9}	0.988	4.271	
B	0.89×10^{-9}	0.987	4.069	$f_D = \dfrac{15.160}{15.384}$
C	0.74×10^{-9}	0.986	3.382	
D	0.54×10^{-9}	0.982	2.463	$f_D = 0.985$
E	0.22×10^{-9}	0.975	0.975	
$J_{BEAM} = 1.0A$				
A	0.62×10^{-9}	0.984	4.254	
B	0.59×10^{-9}	0.983	4.053	$f_D = \dfrac{15.100}{15.384}$
C	0.50×10^{-9}	0.982	3.368	
D	0.36×10^{-9}	0.978	2.453	$f_D = 0.981$
E	0.15×10^{-9}	0.973	0.972	

Figure 5-2 shows a plot of ion beam divergence factor versus ion beam current for the 30-cm E.M. ion thruster. The predicted results from Tables 6 and 7 lie within the data spread obtained from independent experimental determinations. The calculated results are considered most reliable because they are based on data where variables such as grid separation were more easily controlled.

It is interesting to note that the grid set used with the 30-cm E.M. ion thruster is operating below its normalized perveance per hole limit. Figure 4-2 indicates an obtainable normalized perveance per hole limit of 2.3×10^{-9} amp/volt$^{3/2}$ for an accelerator aperture diameter ratio of 0.8. At a beam current of 2.0 ampere the average normalized perveance per hole is 0.89×10^{-9} amp/volt$^{3/2}$, which is also somewhat below the optimum value for ion-optical performance of 1.05×10^{-9} [Figure 4-3]. For this beam current the highest current grid apertures are operating at a normalized perveance per hole of only 1.29×10^{-9} amp/volt$^{3/2}$.

Reducing Accelerator Grid Effective Open Area

Grid sets presently being used in developmental ion thrusters have Small Hole Accelerator Grid (S.H.A.G.) optics. As was previously mentioned in Chapter 4, reducing the accelerator aperture diameter ratio $\frac{d_a}{d_s}$ reduces the loss of un-ionized propellant and improves ion thruster efficiency. However, Figure 5-3 illustrates that reductions in the ratio $\frac{d_a}{d_s}$ significantly decrease the fraction of obtainable Childs' law current density. Figure 5-3 was obtained by varying $\frac{d_a}{d_s}$ for a constant grid separation ratio $\frac{\ell_g}{d_s}$, the resultant changes to the limit of obtainable normalized perveance can then be thought of as changes in the obtainable Childs' law current density for that grid separation ratio.
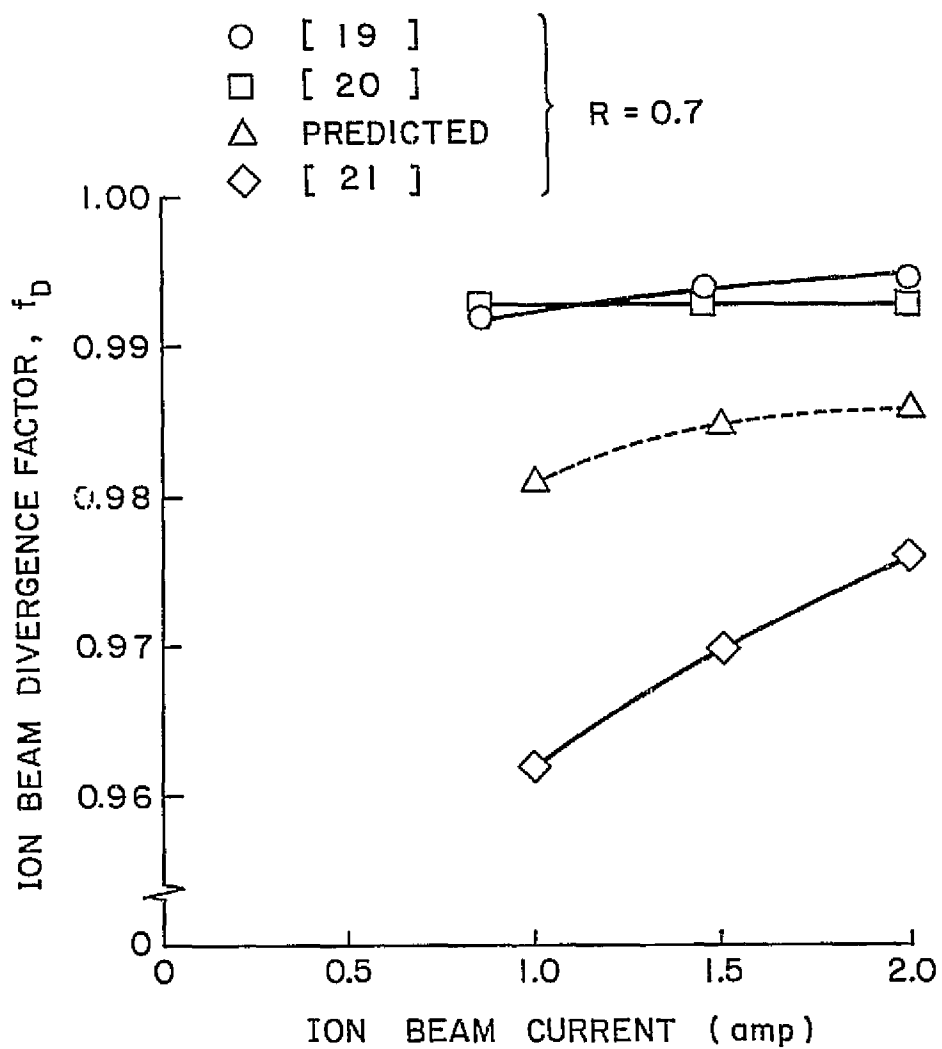
EFFECT OF ACCELERATOR APERTURE DIAMETER
ON EXTRACTED ION CURRENT DENSITY

FIGURE 5-2
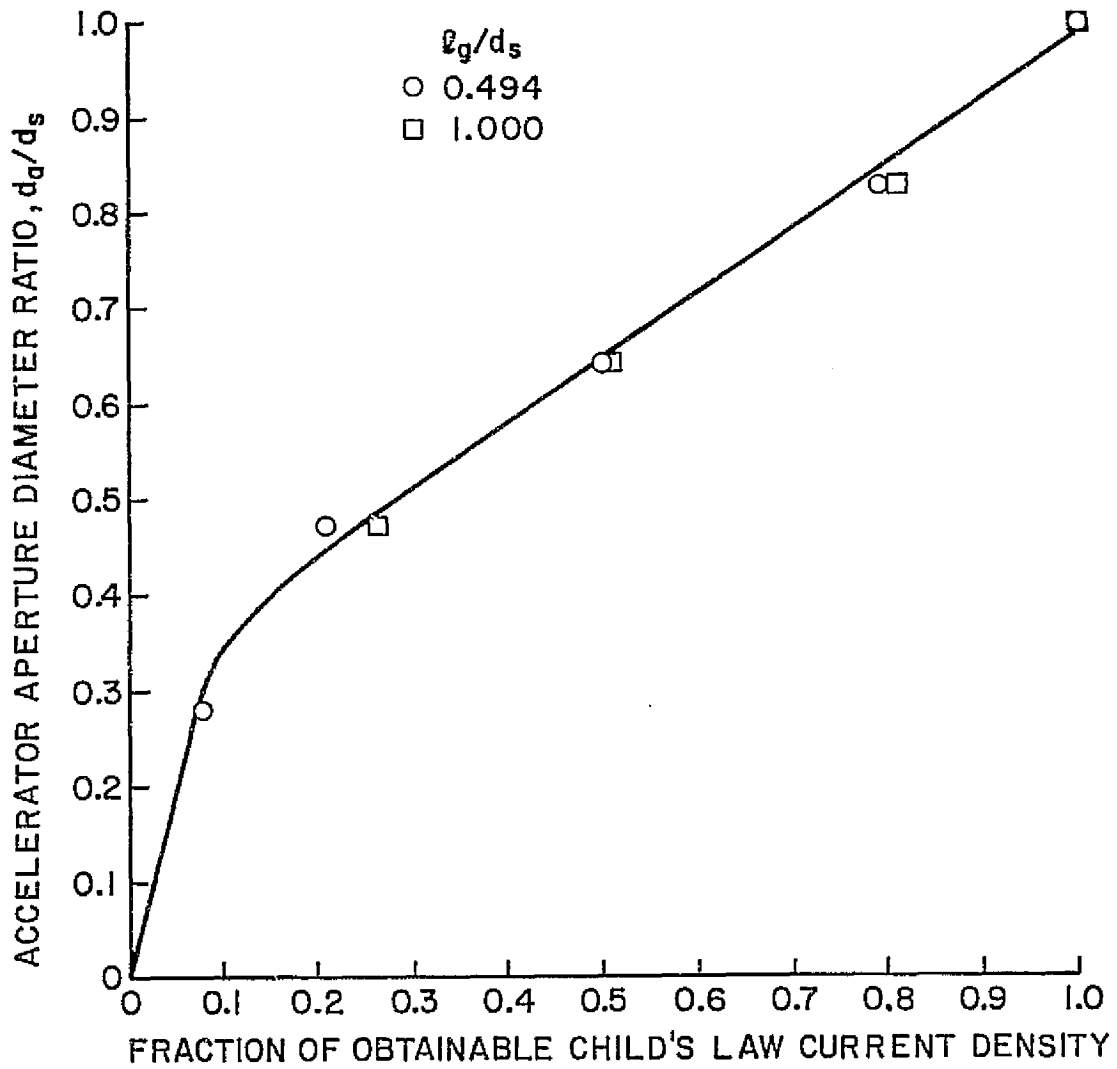
COMPARISON OF PREDICTED AND EXPERIMENTAL
ION BEAM DIVERGENCE (30-cm E.M. ION THRUSTER)

FIGURE 5-3

It was assumed the theoretical normalized perveance per hole limit for mercury, 3.03×10^{-9} amp/volt$^{3/2}$, corresponded to an accelerator aperture diameter ratio of 1.00 (data were obtained which exceeded this theoretical limit [Figure 4-13], however, the discrepancy is thought to be a result of the approximate nature of the one dimensional Childs' current density derivation when used for a two dimensional configuration).

Although accelerator aperture diameter does not appear in Childs' current density law explicity [Equation 1-2], Figure 5-3 reflects the fact that reducing the ratio $\frac{\alpha_a}{d_s}$ causes direct ion impingement on the accelerator grid at lower ion extraction current densities. For example, decreasing the accelerator aperture diameter ratio from 1.000 to 0.642, using the same grid separation ratio, reduces the obtainable Childs' law current density by half [Figure 5-3]. This substantial reduction in ion current density is a detrimental factor in the use of small hole accelerator grids.

The un-ionized propellant atoms which escape through the accelerator grid are in free molecular flow. Under this flow condition, the effective open area each accelerator aperture presents to the escaping propellant atoms is less than its physical open area. The extent of this effective area reduction depends upon the ratio of accelerator grid thickness to accelerator aperture diameter, $\frac{t_a}{d_a}$, and is quantitatively defined by the Clausing factor [22]. Increasing the ratio $\frac{t_a}{d_a}$ decreases the accelerator grid effective open area. Furthermore, previous results show that increasing the accelerator grid thickness (for a constant accelerator aperture diameter) only slightly decreases the limit to the obtainable normalized perveance per hole [Figure 4-4].

As a result, if a set reduction in effective open area is desired, the ion current density which can be extracted using a grid with slightly decreased accelerator aperture diameter and increased accelerator grid thickness is greater than the ion current density which can be extracted using a grid with reduced accelerator aperture diameter only. Table 8 compares this alternate method for reducing the effective accelerator grid open area with the S.H.A.G. optics presently being investigated for the 30-cm ion thruster [23] (the effective reduction in open area and ion current density is determined relative to the standard E.M. accelerator grid geometry whose parameters are $\frac{d_a}{d_s}$ = 0.80 and $\frac{t_a}{d_s}$ = 0.27).

Table 8. ALTERNATE METHOD TO REDUCE THE ACCELERATOR
GRID EFFECTIVE OPEN AREA

	Parameter Varied from Standard E.M. Accelerator Grid	Effective Reduction In Open Area from Standard E.M. Accelerator Grid	Ion Current Density Reduction from Standard E.M. Accelerator Grid
S.H.A.G. Optics	$\frac{d_a}{d_s}$: 0.80 → 0.60	48%	41% [Figure 5-3]
Alternate Method	$\frac{d_a}{d_s}$: 0.80 → 0.70	47%	33% [Figures 5-3 and 4-4]
	$\frac{t_a}{d_s}$: 0.27 → 0.67		

Table 8 shows that 12% more ion current can be obtained by using the alternate method instead of the S.H.A.G. optics to achieve a set reduction in effective accelerator grid open area.

Another advantage to using a thicker accelerator grid is longer accelerator grid lifetime because more grid material is available to

resist ion-sputter erosion [24]. The S.H.A.G. optics have shown an electron backstreaming limit occurring at higher net-to-total accelerating voltage ratios than obtainable with the standard E.M. accelerator grid geometry [14]. An increased electron backstreaming limit would be expected also for a thick accelerator grid, where the negative accellerator potential is more uniformly distributed across each aperture.

CONCLUSION

A detailed experimental investigation has shown that to a good approximation, each geometrical grid parameter independently affects one aspect of ion-optical performance. These trends are listed below.

(i) The magnitudes of ion beam divergence angle and ion beam divergence factor are controlled by variations in the grid separation ratio $\frac{\ell_g}{d_s}$ (at a constant net-to-total accelerating voltage ratio and normalized perveance per hole).

(ii) The limit to the obtainable normalized perveance per hole is controlled by variations in the accelerator aperture diameter ratio $\frac{d_a}{d_s}$.

(iii) The normalized perveance per hole at which the minimum beam divergence angle and maximum beam divergence factor occur is controlled (for a small range of normalized perveance per hole about a value of 1.0×10^{-9} amp/volt$^{3/2}$) by variations in the screen grid thickness ratio $\frac{t_s}{d_s}$.

(iv) Variations in the accelerator grid thickness ratio, $\frac{t_a}{d_s}$, slightly change the overall ion-optical performance.

A graphical technique has been developed incorporating these results which can be used to predict ion-optical performance for an arbitrary ion source and grid set geometry combination.

The graphical results are quite general and may be used for any application where a two-grid optics system is used to produce a broad ion beam.

REFERENCES

1. David L. Lockwood, William Michelsen and Vladimir Hamza, "Analytical Space-Charge Flow and Theoretical Electrostatic Rocket Engine Performance," presented at the Electric Propulsion Conference, Berkley, California, March 14-16, 1962.

2. J. Hyman, Jr., W. O. Eckhardt, R. C. Knechtli and C. R. Buckey, "Formation of Ion Beams from Plasma Sources: Part 1," AIAA Vol. 2, No. 10, pp. 1739-1748, October 1964.

3. Carl D. Bogart and Edward A. Richley, "A Space Charge Flow Computer Program," NASA Tech. Note TN D-3394, 1966.

4. Walter C. Lathem, "Ion Accelerator Designs for Kaufman Thrusters," Journal of Space Craft and Rockets, Vol. 6, No. 11, pp. 1237-1242, November 1969.

5. Harold R. Kaufman, "Accelerator System Solutions for Electron-Bombardment Ion Sources," AIAA paper 75-430, March 1975.

6. David Bohm, "The Characteristics of Electrical Discharges in Magnetic Fields," (A. Guthrie and R. K. Wakerling, ed.), pp. 77-88, McGraw-Hill, New York, 1949.

7. C. D. Child, "Discharge from Hot CaO," Physics Review, Vol. 32, pp. 492-511, 1911.

8. Harold R. Kaufman and Paul D. Reader, "Experimental Performance of Ion Rockets Employing Electron-Bombardment Ion Sources," presented at the ARS Electrostatic Propulsion Conference, U.S. Naval Postgraduate School, Monterey, California, November 3-4, 1960.

9. Paul D. Reader, "Experimental Effects of Scaling on the Performance of Ion Rockets Employing Electron-Bombardment Ion Sources," presented at the National IAS-ARS Joint Meeting, Los Angeles, Calif., June 13-16, 1961.

10. Paul D. Reader, "Investigation of a 10-Centimeter-Diameter Electron-Bombardment Ion Rocket," NASA Tech. Note TN D-1163.

11. John F. Staggs, William P. Gula and William R. Kerslake, "Distribution of Neutral Atoms and Charge-Exchange Ions Downstream of an Ion Thruster," Journal of Space Craft and Rockets, Vol. 5, No. 2, pp. 159-164, February 1968.

12. Harold R. Kaufman, "Technology of Electron-Bombardment Ion Thrusters," Advances in Electronics and Electron Physics, Vol. 36, pp. 327-344, 1974.

13. R. H. Huddlestone and S. L. Leonard, eds., "Plasma Diagnostic Techniques," Pure and Applied Physics, Vol. 21, pp. 537-543, 1965.

14. J. Hyman, Jr., C. R. Dulgeroff, S. Kami and W. S. Williamson, "One Millipound Mercury Ion Thruster," AIAA paper 75-386, March 1975.

15. D. E. Schnelker and C. R. Collet, "30-cm Engineering Model Thruster Design and Qualification Tests," AIAA paper 75-341, March 1975.

16. V. K. Rawlin, B. A. Banks and D. C. Byers, "Design Fabrication, and Operation of Dished Accelerator grids on a 30-cm Ion Thruster," NASA TM X-68013.

17. R. P. Vahrenkamp, private communication.

18. R. L. Poeschel, Private communication.

19. R. L. Poeschel and R. P. Vahrenkamp, "Performance Mapping of a 30-cm Engineering Model Thruster," AIAA paper 75-342, March 1975.

20. J. S. Sovey and H. J. King, "Status of 30-cm Mercury Ion Thruster Development," AIAA paper 74-1117, October 1974.

21. B. Banks, V. Rawlin, A. Weigand and J. Walker, "Direct Thrust Measurements of a 30-cm Ion Thruster," AIAA paper 75-340, March 1975.

22. P. Clausing, Ann. Phys. (Leipzig), Vol. 12, pp. 961-989, 1932.

23. Hughes Research Laboratories, "2.5 KW Advanced Technology Ion Thruster," Contract NAS 3-17831 Monthly Report No. 8, 1 February 1975--1 March 1975.

24. Harold R. Kaufman, "Technology of Electron-Bombardment Ion Thrusters," Advances in Electronics and Electron Physics, Vol. 36, pp. 327-329, 1974.

APPENDIX I

Figure A-1 illustrates the effectiveness of using a screened probe rake for removing low energy charge exchange ions from the primary ion beam. The measured ion beam divergence angle, α, increases by an average of 25% and ion beam divergence factor, f_D, decreases by an average of 0.3% when using an unscreened probe rake. These data were obtained for the high normalized perveance design grid set [Figure 4-1A] but are representative of the trends expected with other grid set geometries. The most significant difference in the beam profile when using an unscreened probe rake was the absence of a zero in ion current for the outer probes. This indicates the large extent of the background charge exchange plasma surrounding the primary ion beam.

EFFECT OF SCREENED FARADAY PROBES ON THE ION BEAM PROFILE

FIGURE A-1
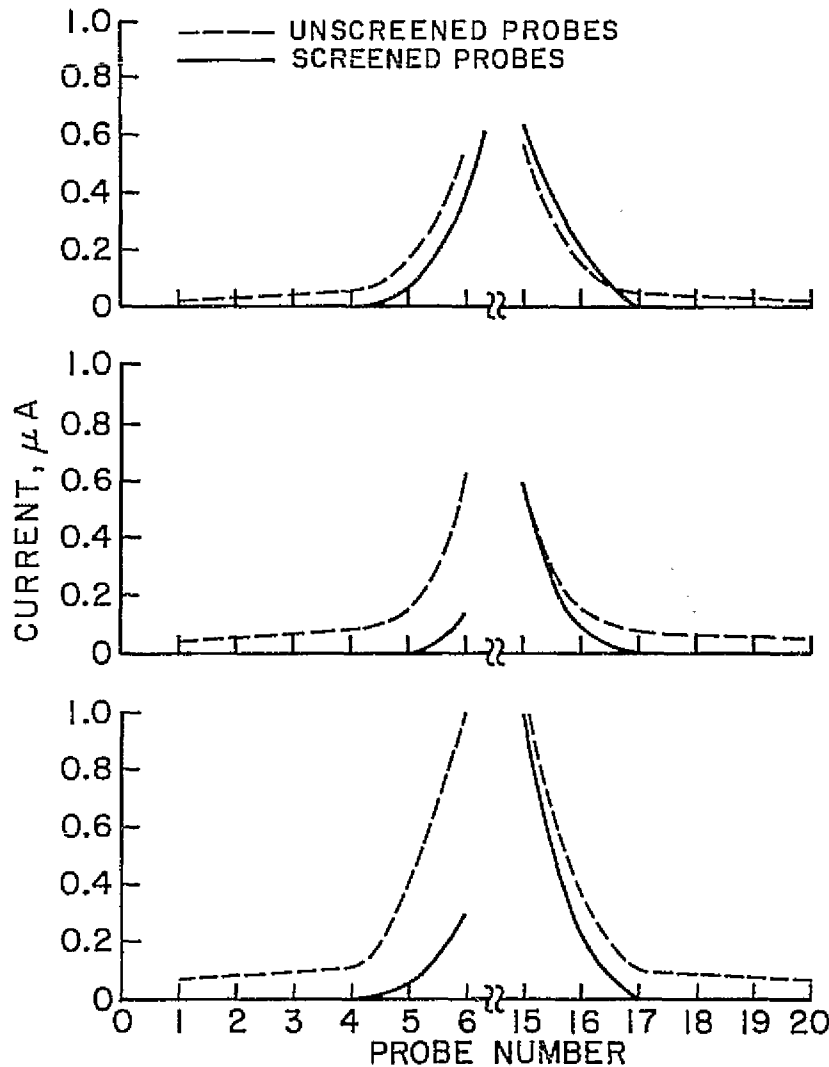
NORMALIZED PERVEANCE = 0.38×10^{-9} (amp/volt$^{3/2}$)

	UNSCREENED	SCREENED
α	15.9°	13.5°
f_D	0.9852	0.9880

NORMALIZED PERVEANCE = 1.00×10^{-9} (amp/volt$^{3/2}$)

	UNSCREENED	SCREENED
α	13.5°	10.3°
f_D	0.9901	0.9917

NORMALIZED PERVEANCE = 1.50×10^{-9} (amp/volt$^{3/2}$)

	UNSCREENED	SCREENED
α	14.2°	10.9°
f_D	0.9893	0.9930

61

APPENDIX II

The ion beam divergence angle, α, and the ion beam divergence factor, f_D, were calculated from the probe rake data assuming an ion beam point source and circular symmetry for each ion beam profile. The following equations were used in their determination

$$\alpha = \text{Arctan}\left(\frac{R_\alpha}{17.5}\right)$$

$$f_D = \frac{\sum\limits_{i=1}^{77} J_i \cdot R_i \cos\Theta_i}{\sum\limits_{i=1}^{77} J_i R_i}$$

where

R_α = radius normal to the beam axis defining a cone enclosing 95% of the total integrated beam current (the probe rake was positioned 17.5 cm downstream of the ion source)

J_i = probe current for the ith probe (an interpolation routine was used to increase the effective number of probe data points from 20 to 77)

R_i = distance from the ith probe to the ion beam axis

Θ_i = angle formed by intersection of a line extending from the center of the ion source grid set to the ith probe and the ion beam axis.

APPENDIX III

Experimental Results

R	$\frac{\ell_g}{d_s}$	$\frac{d_a}{d_s}$	$\frac{t_s}{d_s}$	$\frac{t_a}{d_s}$	$J^*/V_t^{3/2}$ (nanopervs/hole)	$J/V_t^{3/2}(\frac{\ell_e}{d_s})^2$ (nanopervs/hole)	α (deg.)	f_D
0.7	0.247	0.642	0.185	0.370	0.302	0.094	23.29	0.9682
					0.958	0.298	22.26	0.9731
					1.598	0.497	20.34	0.9785
					2.190	0.681	17.83	0.9821
					2.813	0.875	16.47	0.9844
					⸱ ⸳21	1.064	16.19	0.9849
					4.074	1.267	16.16	0.9843
					4.698	1.461	16.46	0.9826
					5.353	1.665	16.95	0.9793
0.5	0.494	0.642	0.185	0.370	0.304	0.150	22.74	0.9686
					0.640	0.316	21.55	0.9724
					0.960	0.474	20.37	0.9748
					1.279	0.632	19.52	0.9760
					1.599	0.790	19.03	0.9776
					1.887	0.932	18.75	0.9790
					2.190	1.082	18.38	0.9799
					2.494	1.232	18.13	0.9801

* Both perveance and normalized perveance per hole have been corrected for use with mercury propellant.

R	$\frac{\ell_g}{d_s}$	$\frac{d_a}{d_s}$	$\frac{t_s}{d_s}$	$\frac{t_a}{d_s}$	$J/V_t^{3/2}$ (nanopervs/ hole)	$J/V_t^{3/2}(\frac{\ell_e}{d_s})^2$ (nanopervs/ hole)	α (deg.)	f_D
0.5	0.494	0.642	0.185	0.370	2.814	1.390	17.91	0.9798
					3.053	1.508	17.83	0.9790
0.7					0.304	0.150	19.40	0.9765
					0.640	0.316	18.41	0.9802
					0.960	0.474	17.15	0.9835
					1.279	0.632	15.04	0.9867
					1.599	0.790	13.43	0.9888
					1.887	0.932	13.17	0.9897
					2.190	1.082	13.52	0.9895
					2.494	1.232	14.00	0.9889
					2.814	1.390	14.59	0.9878
					3.053	1.508	15.08	0.9864
0.9					0.304	0.150	17.47	0.9804
					0.640	0.316	16.44	0.9845
					0.960	0.474	14.39	0.9896
					1.279	0.632	10.85	0.9932
					1.599	0.790	9.10	0.9947
					1.887	0.932	8.56	0.9952
					2.190	1.082	8.46	0.9953
					2.494	1.232	8.79	0.9950
					2.814	1.390	9.45	0.9944
					3.132	1.547	10.11	0.9932
0.5	0.741	0.642	0.185	0.370	0.154	0.123	19.78	0.9749
					0.398	0.318	18.74	0.9783

R	$\dfrac{\ell_g}{d_s}$	$\dfrac{d_a}{d_s}$	$\dfrac{t_s}{d_s}$	$\dfrac{t_a}{d_s}$	$J/V_t^{3/2}$ (nanopervs/ hole)	$J/V_t^{3/2}\left(\dfrac{\ell_e}{d_s}\right)^2$ (nanopervs/ hole)	α (deg.)	f_D
0.5	0.741	0.642	0.185	0.370	0.640	0.511	18.00	0.9807
					0.879	0.702	16.12	0.9834
					1.119	0.894	15.41	0.9850
					1.358	1.085	15.70	0.9854
					1.598	1.277	16.34	0.9848
					1.886	1.507	17.64	0.9821
0.7					0.154	0.123	17.07	0.9805
					0.398	0.318	16.08	0.9838
					0.640	0.511	14.89	0.9870
					0.879	0.702	12.80	0.9899
					1.119	0.894	11.58	0.9914
					1.353	1.085	11.46	0.9920
					1.598	1.277	11.88	0.9916
					1.817	1.452	12.39	0.9909
					1.967	1.572	13.22	0.9894
0.9					0.154	0.123	15.37	0.9835
					0.398	0.318	14.28	0.9871
					0.640	0.511	12.40	0.9931
					0.879	0.702	9.71	0.9942
					1.119	0.894	7.84	0.9956
					1.358	1.085	7.49	0.9959
					1.598	1.277	7.84	0.9956
					1.817	1.452	8.09	0.9954
					1.967	1.572	8.54	0.9948

66

R	$\frac{\ell_g}{d_s}$	$\frac{d_a}{d_s}$	$\frac{t_s}{d_s}$	$\frac{t_a}{d_s}$	$J/V_t^{3/2}$ (nanopervs/ hole)	$J/V_t^{3/2}(\frac{\ell_e}{d_s})^2$ (nanopervs/ hole)	α (deg.)	f_D
0.5	1.000	0.642	0.185	0.370	0.078	0.098	17.33	0.9794
					0.234	0.292	16.03	0.9827
					0.398	0.497	15.12	0.9851
					0.559	0.699	14.30	0.9867
					0.719	0.899	12.99	0.9885
					0.879	1.099	13.06	0.9892
					1.038	1.298	14.01	0.9885
					1.179	1.474	15.35	0.9861
0.7					0.078	0.098	14.98	0.9842
					0.234	0.292	13.66	0.9872
					0.398	0.497	12.98	0.9892
					0.559	0.699	11.59	0.9915
					0.719	0.899	10.36	0.9931
					0.879	1.099	10.14	0.9936
					1.038	1.298	10.54	0.9933
					1.246	1.558	11.45	0.9920
0.9					0.078	0.098	13.28	0.9870
					0.234	0.292	12.36	0.9894
					0.398	0.497	11.16	0.9919
					0.559	0.699	9.56	0.9914
					0.719	0.899	7.53	0.9960
					0.879	1.099	6.95	0.9965
					1.038	1.298	7.04	0.9965
					1.278	1.598	7.80	0.9958

R	$\dfrac{\ell_g}{d_s}$	$\dfrac{d_a}{d_s}$	$\dfrac{t_s}{d_s}$	$\dfrac{t_a}{d_s}$	$J/V_t^{3/2}$ (nanopervs/ hole)	$J/V_t^{3/2}\left(\dfrac{\ell_e}{d_s}\right)^2$ (nanopervs/ hole)	α (deg.)	f_D
0.7	0.494	0.278	0.185	0.370	0.079	0.039	21.34	0.9716
					0.154	0.076	20.98	0.9741
					0.232	0.115	20.45	0.9775
					0.304	0.150	17.96	0.9840
					0.399	0.197	10.60	0.9919
					0.472	0.233	8.36	0.9946
0.7	0.494	0.469	0.185	0.370	0.154	0.076	20.73	0.9730
					0.304	0.150	20.41	0.9743
					0.476	0.235	19.79	0.9762
					0.640	0.316	19.41	0.9777
					0.800	0.395	19.01	0.9791
					0.960	0.474	18.34	0.9812
					1.119	0.553	16.80	0.9843
					1.279	0.632	14.20	0.9878
0.5	0.494	0.827	0.185	0.370	0.304	0.150	22.79	0.9690
					0.800	0.395	21.12	0.9738
					1.279	0.632	19.64	0.9763
					1.745	0.862	19.05	0.9785
					2.190	1.082	18.51	0.9796
					2.653	1.311	18.39	0.9792
					3.131	1.547	18.42	0.9783
					3.557	1.757	18.64	0.9767
					4.075	2.013	19.33	0.9741
					4.395	2.171	19.99	0.9715

R	$\dfrac{\ell_g}{d_s}$	$\dfrac{d_a}{d_s}$	$\dfrac{t_s}{d_s}$	$\dfrac{t_a}{d_s}$	$J/V_t^{3/2}$ (nanopervs/ hole)	$J/V_t^{3/2}\left(\dfrac{\ell_e}{d_s}\right)^2$ (nanopervs/ hole)	α (deg.)	f_D
0.7	0.494	0.827	0.185	0.370	0.304	0.150	19.13	0.9774
					0.800	0.395	17.89	0.9823
					1.279	0.632	14.95	0.9871
					1.745	0.862	13.60	0.9892
					2.190	1.082	14.07	0.9889
					2.653	1.311	14.77	0.9877
					3.131	1.547	15.41	0.9861
					3.557	1.757	15.72	0.9847
					4.075	2.013	16.04	0.9827
					4.866	2.404	17.00	0.9776
0.9					0.304	0.150	17.56	0.9805
					0.800	0.395	15.80	0.9870
					1.279	0.632	11.68	0.9925
					1.745	0.862	9.47	0.9944
					2.190	1.082	9.17	0.9947
					2.653	1.311	9.78	0.9940
					3.131	1.547	10.42	0.9932
					3.557	1.757	10.99	0.9921
					4.075	2.013	11.90	0.9903
					5.034	2.487	14.05	0.9853
0.5	0.494	0.642	0.062	0.370	0.304	0.150	22.99	0.9690
					0.800	0.395	22.44	0.9717
					1.279	0.632	21.24	0.9740
					1.745	0.862	19.37	0.9972

R	$\frac{\ell_g}{d_s}$	$\frac{d_a}{d_s}$	$\frac{t_s}{d_s}$	$\frac{t_a}{d_s}$	$J/V_t^{3/2}$ (nanopervs/ hole)	$J/V_t^{3/2}(\frac{\ell_e}{d_s})^2$ (nanopervs/ hole)	α (deg.)	f_D
0.5	0.494	0.642	0.062	0.370	2.190	1.082	18.02	0.9795
					2.653	1.311	17.68	0.9802
					3.131	1.547	17.65	0.9797
					3.491	1.725	17.97	0.9779
0.7					0.304	0.150	21.77	0.9737
					0.800	0.395	20.31	0.9783
					1.279	0.632	18.19	0.9834
					1.745	0.862	14.95	0.9876
					2.190	1.082	13.61	0.9890
					2.653	1.311	13.73	0.9889
					3.131	1.547	14.23	0.9878
					3.557	1.757	15.00	0.9852
0.9					0.304	0.150	19.30	0.9793
					0.800	0.395	17.28	0.9852
					1.279	0.632	14.50	0.9905
					1.745	0.862	10.48	0.9936
					2.190	1.082	9.21	0.9947
					2.653	1.311	8.97	0.9948
					3.131	1.547	9.48	0.9942
					3.628	1.792	10.41	0.9924
0.7	0.494	0.642	0.123	0.370	0.304	0.150	22.07	0.9725
					0.800	0.395	19.96	0.9787
					1.279	0.632	18.04	0.9831
					1.745	0.862	15.22	0.9869

R	$\frac{\ell_g}{d_s}$	$\frac{d_a}{d_s}$	$\frac{t_s}{d_s}$	$\frac{t_a}{d_s}$	$J/V_t^{3/2}$ (nanopervs/ hole)	$J/V_t^{3/2}(\frac{\ell_e}{d_s})^2$ (nanopervs/ hole)	α (deg.)	f_D
0.7	0.494	0.642	0.123	0.370	2.190	1.082	14.54	0.9880
					2.653	1.311	14.78	0.9879
					3.131	1.547	15.18	0.9870
					3.628	1.792	15.73	0.9846
0.7	0.494	0.642	0.247	0.370	0.304	0.150	20.52	0.9745
					0.640	0.316	19.39	0.9785
					0.960	0.474	18.28	0.9824
					1.279	0.632	16.50	0.9854
					1.599	0.790	14.76	0.9877
					1.887	0.932	13.96	0.9889
					2.190	1.082	13.89	0.9890
					2.494	1.232	14.24	0.9886
					2.811	1.389	14.78	0.9877
					3.053	1.508	15.57	0.9858
0.7	0.494	0.642	0.185	0.123	0.304	0.150	19.80	0.9757
					0.640	0.316	18.97	0.9792
					0.960	0.474	17.66	0.9832
					1.279	0.632	15.18	0.9870
					1.599	0.790	13.57	0.9893
					1.887	0.932	13.27	0.9901
					2.190	1.082	13.49	0.9900
					2.494	1.232	13.83	0.9896
					2.811	1.389	14.42	0.9886
					3.132	1.547	15.47	0.9858

R	$\frac{\ell_g}{d_s}$	$\frac{d_a}{d_s}$	$\frac{t_s}{d_s}$	$\frac{t_a}{d_s}$	$J/V_t^{3/2}$ (nanopervs/ hole)	$J/V_t^{3/2}(\frac{\ell_e}{d_s})^2$ (nanopervs/ hole)	α (deg.)	f_D
0.7	0.494	0.642	0.185	0.617	0.304	0.150	19.93	0.9754
					0.640	0.316	18.98	0.9786
					0.960	0.474	17.93	0.9818
					1.279	0.632	16.12	0.9849
					1.599	0.790	14.57	0.9874
					1.887	0.932	14.23	0.9883
					2.190	1.082	14.37	0.9884
					2.494	1.232	15.03	0.9876
					2.654	1.311	15.51	0.9864
0.5	0.494	0.642	0.185	0.864	0.304	0.150	23.06	0.9676
					0.640	0.316	22.17	0.9701
					0.960	0.474	21.37	0.9720
					1.279	0.632	20.08	0.9738
					1.599	0.790	18.98	0.9759
					1.887	0.932	18.65	0.9772
					2.190	1.082	18.72	0.9777
					2.397	1.184	18.70	0.9775
0.7					0.304	0.150	20.07	0.9752
					0.640	0.316	19.03	0.9783
					0.960	0.474	17.76	0.9815
					1.279	0.632	16.08	0.9844
					1.599	0.790	14.54	0.9866
					1.887	0.932	14.17	0.9874
					2.190	1.082	14.29	0.9874

R	$\dfrac{\ell_g}{d_s}$	$\dfrac{d_a}{d_s}$	$\dfrac{t_s}{d_s}$	$\dfrac{t_a}{d_s}$	$J/V_t^{3/2}$ (nanopervs/ hole)	$J/V_t^{3/2}(\dfrac{\ell_e}{d_s})^2$ (nanopervs/ hole)	α (deg.)	f_D
0.7	0.494	0.642	0.185	0.864	2.417	1.194	14.66	0.9866
0.9					0.304	0.150	17.95	0.9793
					0.640	0.316	16.98	0.9829
					0.960	0.474	15.30	0.9874
					1.279	0.632	12.34	0.9911
					1.599	0.790	10.05	0.9933
					1.887	0.932	9.71	0.9937
					2.190	1.082	9.82	0.9935
					2.502	1.263	10.68	0.9923